Achieving DFT accuracy in short range ordering and stacking fault energy using moment tensor potential for CoCrFeNi and CoCrNi

Mashroor S. Nitol,[1,*] Artur Tamm,[2] Subah Mubassira,[3] Shuozhi Xu,[3] and Saryu J. Fensin[1]
[1]*Center for Integrated Nanotechnologies, Los Alamos National Laboratory, Los Alamos, New Mexico 87544, USA*
[2]*Institute of Physics, University of Tartu, 50411 Tartu, Estonia*
[3]*School of Aerospace and Mechanical Engineering, University of Oklahoma, Norman, Oklahoma 73019-1052, USA*

(Received 16 October 2025; revised 1 April 2026; accepted 15 April 2026; published 8 May 2026)

A Moment Tensor Potential (MTP) is developed for equiatomic CoCrNi and CoCrFeNi alloys to enable large-scale simulations of chemical short-range order (CSRO) and defect energetics with near density functional theory (DFT) accuracy. The training database includes unary to quaternary configurations as well as DFT derived short-range ordered structures, ensuring accurate representation of thermodynamically relevant chemical environments. The MTP reproduces DFT energies, forces, stresses, and elastic constants across diverse compositions and phases. Hybrid Monte Carlo/molecular dynamics simulations recover key CSRO trends, including Cr–Cr and Fe–Fe repulsion and Ni–Cr ordering, with correct sign structure across temperature. Intrinsic stacking fault (ISF) energies are predicted to be 54 mJ/m^2 for CoCrNi and 36 mJ/m^2 for CoCrFeNi, consistent with DFT trends and sensitive to local chemical fluctuations. The potential further enables simulations of solute segregation at grain boundaries while preserving structural units. The developed MTP enables transferable, physically consistent simulations of thermodynamic stability and defect mediated mechanical response in fcc medium entropy alloys across extended length and timescales.

DOI: 10.1103/nqsc-gzkw

I. INTRODUCTION

Medium-entropy alloys (MEAs) represent a transformative approach to alloy design, characterized by the incorporation of three or four principal elements in near-equiatomic ratios, each typically occupying 5–35 at. % [1,2]. The medium configurational entropy promotes the stabilization of simple solid solution phases, often with face-centered cubic (fcc) or body-centered cubic (bcc) structures rather than complex intermetallic compounds [3]. Among MEAs, the equiatomic CoCrFeNi and CoCrNi alloys have emerged as model systems due to their exceptional combination of mechanical strength, ductility, thermal stability, and corrosion resistance. These attributes make these alloys promising candidates for demanding applications, including cryogenic structural components, energy systems, and next generation aerospace materials [4,5].

The microstructure of CoCrFeNi and CoCrNi is predominantly a single phase fcc solid solution with a random distribution of constituent elements [6,7]. This phase stability arises from the medium entropy of mixing, which suppresses the formation of intermetallic compounds and promotes a homogeneous structure even after prolonged thermal exposure [8,9]. As-cast CoCrFeNi typically exhibits a dendritic morphology, and at finer scales, nanoprecipitates may form as a result of sluggish atomic diffusion inherent to MEAs [10,11]. The alloy retains a stable fcc lattice across a broad temperature range [12,13], with deformation mechanisms dominated by dislocation slip and nanotwinning, particularly under cryogenic conditions. This microstructural simplicity, combined with complex atomic-scale interactions, underpins its remarkable mechanical performance and makes it an ideal platform for studying fundamental processes in multicomponent metallic systems [14,15].

Extensive first principles calculations based on density functional theory (DFT) have been conducted to investigate the fundamental properties of CoCrFeNi and CoCrNi [16–25]. In particular, the energetics of point defects and small vacancy clusters have been evaluated to understand defect stability and migration behavior. These studies have revealed unique characteristics in defect interactions, which are significantly influenced by the complex chemical disorder inherent in the alloy. It was demonstrated that CoCrFeNi and CoCrNi possess enhanced irradiation resistance due to the difficulty of vacancy cluster formation [26,27]. Binding energy calculations indicated that di-vacancy clusters are marginally stable, while trivacancy clusters are unstable, limiting the growth of larger vacancy clusters and suppressing void swelling [28,29]. Furthermore, thermodynamic modeling revealed that phase stability is governed not solely by configurational entropy but also by significant contributions from vibrational, electronic, and magnetic entropies [30]. Thermal expansion and bulk modulus predictions showed good agreement with experimental data, confirming the robustness of the first principles approach [31]. Despite these insights, the inherent limitations of DFT in exploring large scale behavior, such as microstructural evolution under extended irradiation or mechanical loading, remain pronounced. The atomistic models used in DFT are restricted to supercells of a few hundred atoms due to computational expense, thereby limiting accessible timescales, defect concentrations, and chemical fluctuation statistics.

*Contact author: mash@lanl.gov

Classical interatomic potentials, such as the embedded atom method (EAM) [32], modified embedded atom method (MEAM) [33], and Lennard-Jones (LJ) [34] potentials, have therefore been employed to extend simulations to larger scales. MEAM-based molecular dynamics (MD) simulations have successfully captured important metallurgical phenomena in multicomponent alloys, including sluggish diffusion and deformation twinning at cryogenic temperatures [35]. However, MEAM potentials are typically parameterized using binary interactions and then extrapolated to multicomponent systems, an assumption that may introduce inaccuracies when local chemical complexity becomes dominant. Similarly, LJ-type effective pair potentials have provided simplified frameworks for CoCrFeMnNi alloys [36], reproducing certain qualitative trends in elastic constants and stacking fault behavior. Nevertheless, the pairwise functional form limits the accurate description of many-body interactions, local chemical short range order (CSRO), and defect energetics. Despite their computational efficiency, classical EAM and MEAM potentials often struggle to simultaneously reproduce elastic properties, stacking fault energies, vacancy formation energies, and phase stability across the full compositional space of CoCrFeNi alloys. Their fixed functional forms constrain the representation of highly anharmonic and chemically disordered energy landscapes, which are intrinsic to medium and high entropy alloys. As a result, predictions of defect cluster stability, segregation tendencies, and thermodynamic driving forces may remain semiquantitative.

Recent advances in machine learning (ML)-based interatomic potentials have provided a promising route to overcome these limitations [37–44]. Several classes of ML potentials exist, including neural network potentials [45], Gaussian approximation potentials (GAP) [46], spectral neighbor analysis potentials [47], and moment tensor potentials (MTPs) [48]. Among these, the MTP framework has demonstrated an effective balance between quantum mechanical accuracy and computational efficiency [44,49–53]. MTPs systematically approximate the potential energy surface using a hierarchy of tensorial descriptors fitted to first principles datasets, enabling accurate representation of many body interactions and complex local environments [54].

A recent MTP potential developed for the CoCrNi system [55] (hereafter referred to as MTP-Cao) was trained exclusively on ternary CoCrNi configurations with a focus on reproducing CSRO and generalized stacking fault energies. While that work demonstrated the capability of MTPs to capture targeted properties within a restricted compositional space, its transferability to unary, binary, and quaternary environments, as well as to defect and surface configurations, was not systematically assessed.

In the present work, MTPs for CoCrNi and CoCrFeNi were constructed using a systematically expanded training database incorporating unary, binary, ternary, and quaternary configurations. This expanded dataset includes equilibrium structures, strained states, defective configurations, and thermally sampled environments, ensuring robust coverage of the relevant configurational space. The inclusion of unary structures was found to be critical for properly constraining elemental energetics, improving phase stability predictions, and ensuring reliable extrapolation to dilute solute concentrations and defect configurations.

To rigorously evaluate transferability, the developed MTPs are benchmarked not only against DFT calculations but also against representative EAM [56], MEAM [35], and the recently published MTP-Cao [55] potential. This comparative assessment enables a quantitative evaluation of improvements in elastic constants, surface energies, vacancy formation energies, phonon dispersions, stacking fault energies, decohesion behavior, and phase stability.

II. METHODS

A. DFT training database

To develop a transferable and accurate ML interatomic potential for the CoCrFeNi system, an extensive DFT database was constructed. The database was systematically designed to span a wide range of atomic environments, including unary, binary, ternary, quaternary compositions, while capturing both harmonic and anharmonic atomic behaviors across diverse structural and chemical configurations.

For the elemental constituents Co, Cr, Fe, and Ni, a comprehensive set of relaxed crystalline structures was generated. The structural prototypes considered included fcc, bcc, hexagonal close-packed (hcp), simple cubic, ω phase, A15, diamond cubic, and β-Sn. Each structure was fully relaxed to obtain equilibrium configurations. To incorporate anharmonic effects and thermal fluctuations, perturbations were introduced around equilibrium atomic positions following the methodology of [43]. Small random displacements were applied to emulate vibrational motion at finite temperatures, thereby improving the transferability of the trained potential across both harmonic and anharmonic regimes. In addition, surface structures were generated to capture low-coordination atomic environments. Symmetric, non-polar slab models were systematically constructed for each phase using the Pymatgen library [57], with Miller indices enumerated up to a predefined maximum value. Elastic properties were also included by applying finite distortions to the relaxed bulk structures with the `elastic_vasp` package [58,59]. Stress tensors were obtained via DFT, and the independent elastic constants were extracted according to crystal symmetry, thereby embedding mechanical response information in the dataset. To ensure accurate cohesive energies, isolated atom calculations were also performed for each constituent element.

Binary intermetallic structures were then generated for all unique elemental pairs. Although no stable intermetallics exist in the CoCrFeNi system, a wide range of prototype binary structures was considered to constrain the ML potential to reproduce the positive mixing enthalpies correctly. These prototypes included B2, Ba, B19 and its derivative B19′, B20, B32, B33, B81, $L1_0$, Al_3Os_2, B82, C1, C14, C22, C38, C40, Cmcm, $D1_a$, $D5_a$, DO_{19}, DO_{22}, DO_{23}, DO_{24}, and $L1_2$. Unless otherwise required by prototype stoichiometry, equiatomic compositions were adopted. To capture finite-temperature effects, $3 \times 3 \times 3$ supercells of low-energy phases were constructed, including fcc and Co (hcp), Cr (bcc) and Fe (bcc), and Ni (fcc). Solute atoms were then substituted at concentrations ranging from 1 to 50 at. % in increments of 5%. Each

configuration was thermally perturbed by random displacements up to 0.6 Å, following previous work by [53]. To further enrich the sampling, isotropic strains of ±5% were applied, and for each strain state, 25 distinct thermally perturbed configurations were generated. In this way, solute host systems were comprehensively explored, including Co-rich [Co–Cr, Co–Fe, Co–Ni in fcc/Co (hcp)], Cr-rich [Cr–Co, Cr–Fe, Cr–Ni in Cr (bcc)], Fe-rich [Fe–Co, Fe–Cr, Fe–Ni in Fe (bcc)], and Ni-rich [Ni–Co, Ni–Cr, Ni–Fe in Ni (fcc)] environments. This approach ensured robust performance across a wide range of binary alloy compositions and atomic environments.

To further enhance the interpolation capability across multicomponent systems, ternary equiatomic structures were generated. The ternary dataset consists exclusively of chemically ordered equiatomic concentrations. For instance, the CoCrNi ternary system was constructed using representative phases of its constituents, namely, Co (hcp and fcc), Cr (bcc), and Ni (fcc). These structures were relaxed and subsequently perturbed in an analogous manner to the binary dataset to emulate thermal fluctuations. Finally, quaternary datasets were prepared for the equiatomic CoCrFeNi alloy, with relaxed fcc structures serving as the basis for additional thermal perturbations. To explicitly capture CSRO, DFT-informed MC configurations [60] were also incorporated into the training database, ensuring accurate representation of thermodynamically relevant ordered states.

All DFT calculations were carried out using the Vienna Ab initio Simulation Package [61], version 6.3.2, using the Perdew Burke Ernzerhof generalized gradient approximation for exchange correlation [62]. A plane wave energy cutoff of 520 eV was used, with electronic self consistency achieved to within 10^{-6} eV. Partial occupancies were treated with Gaussian smearing of width 0.2 eV, and Brillouin zone integrations used a Γ-centered Monkhorst Pack k-point grid with spacing of 0.02 $Å^{-1}$. All calculations included spin polarization. At low temperature, DFT predicts weak ferromagnetism (FM) in CoCrNi and more complex magnetic frustration in CoCrFeNi, primarily due to the antiferromagnetic (AFM) tendencies of Cr. With increasing temperature, magnetic order weakens and both alloys approach a disordered magnetic state above their Curie temperatures, which are generally in the few hundred Kelvin range depending on composition and local chemical order. Because the MTP captures magnetic effects implicitly through spin polarized DFT training data but does not model spin fluctuations explicitly, it is most reliable in temperature regimes where no qualitative magnetic phase transition occurs. In practice, this includes (i) 0 K mechanical property calculations referenced to the magnetic DFT ground state and (ii) intermediate to high temperatures ($\geqslant$ 1200 K), where magnetic disorder dominates and magnetic contributions are effectively averaged. Near magnetic transition temperatures, the absence of explicit spin variables may limit quantitative accuracy for magnetically driven thermodynamic anomalies.

B. Moment tensor potential

At its core, MTP represents the local atomic environment through moment tensors $M_{\mu,\nu}$, defined as

$$M_{\mu,\nu}(\mathbf{n_i}) = \sum f_\mu(|\mathbf{r}_{ij}|, z_i, z_j)\, \mathbf{r}_{ij} \otimes \ldots \otimes \mathbf{r}_{ij}, \qquad (1)$$

where $\mathbf{n}_i$ denotes the neighborhood of atom i, comprising the relative positions $\mathbf{r}_{ij}$ and types z_j of neighboring atoms. The position vector $\mathbf{r}_{ij}$ points from atom i to atom j, while z_i and z_j represent the atomic species of atom i and its neighbor, respectively. Radial dependencies are captured by the functions f_μ, whereas angular information is encoded via the tensor product ($\otimes$) of multiple $\mathbf{r}_{ij}$ vectors, resulting in a rank-ν tensor. The cutoff radius r_c defines the maximum spatial range of interactions, while the maximum level of basis expansion (lev_{max}, an even integer typically between 2 and 28) controls the model's expressiveness by regulating the number of tensorial basis functions. During training, the objective function assigned different weights to each target quantity, with $w_e = 1$ for energies, $w_f = 0.01$ for forces, and $w_s = 0.001$ for stresses, thereby prioritizing energy accuracy while still incorporating force and stress information to improve transferability. This weighting strategy ensured that the potential could accurately capture both local atomic environments and global energy trends. A 90:10 split between training and validation datasets was used to optimize fitting quality while monitoring overfitting. All MTP fitting, validation, and deployment were carried out using the MLIP package [54] within the LAMMPS framework [63]. Postprocessing, trajectory analysis, and visualization of atomic configurations were performed using OVITO [64].

Following the recent methodology used for developing a Ti-Al-V potential within the MTP framework [53], a similar approach was adopted in this work. A level-20 MTP basis was selected after comparison with level-18 models, yielding the lowest validation errors. The minimal cutoff radius, r_{min}, was initially set to 2.0 Å and was adaptively updated during training, allowing the potential to dynamically capture short-range interactions critical for accurately modeling highly stressed atomic configurations. To optimize the maximum cutoff radius, r_{max} was varied from 5.0 to 6.0 Å in 0.1 Å increments. For each combination of basis level and r_{max}, 20 models were trained with randomized initializations, resulting in a total of 400 models (2 levels × 10 cutoff values × 20 random seeds). Model selection was based on the lowest validation errors for both unary elastic constants and force predictions on quaternary datasets.

III. RESULT

A. Unary elements

Validation of unary elemental properties constitutes a fundamental prerequisite for assessing the transferability of any interatomic potential in multicomponent systems. Accurate reproduction of lattice parameters, elastic constants, and relative phase energetics of the constituent elements ensures that elemental bonding characteristics and mechanical responses are properly constrained prior to modeling chemically complex alloys. Inadequate description of unary energetics can propagate systematic errors into predictions of defect formation energies, stacking fault energetics, and phase stability in higher order compositions. Therefore, comprehensive benchmarking against DFT for Co, Cr, Fe, and Ni provides a strong baseline test of physical fidelity before extending the analysis to binary, ternary, and quaternary configurations. Unlike classical potentials such as MEAM, where unary, binary, and

ternary interactions can often be parameterized or tuned separately, machine learning interatomic potentials are trained through a global optimization over the entire database. In the ML framework, all configurations contribute simultaneously to the fitted energy landscape, and inaccuracies in elemental energetics may propagate nonlinearly into multicomponent predictions. Although some recent ML potential developments attempt to minimize the training database by focusing primarily on target alloy compositions, such reduction may compromise physical consistency and limit transferability beyond the fitted configurational space [65,66]. In the present work, explicit inclusion of comprehensive unary datasets ensures that elemental bonding characteristics and phase stability trends are rigorously constrained, thereby enhancing the robustness and predictive reliability of the potential across binary, ternary, and quaternary environments. For consistency in the comparative analysis of classical potentials, the EAM results reported here are from two different potentials: Co, Cr, and Ni properties are evaluated using the CoCrNi potential of [56], whereas Fe properties are obtained from the CoCrFeNi potential of [67].

1. Elastic properties

Table I summarizes the structural and elastic properties of the elemental constituents predicted by the present MTP in comparison with DFT, EAM, MEAM, and MTP-Cao. The equilibrium lattice parameters predicted by MTP deviate from DFT by less than 1% for all elemental phases, comparable to or better than classical potentials. This indicates that the equilibrium volumes are well constrained in the training process.

A more rigorous test of transferability is provided by the elastic constants. To quantify accuracy, relative percentage errors were evaluated for each independent elastic component with respect to DFT values. Across all unary phases, the present MTP exhibits typical elastic constant errors within 2–8%, with an average deviation below 6%. For Co (hcp), the majority of elastic components are reproduced within approximately 5% relative error, including the cross term C_{13}, which is often poorly described by empirical potentials. In contrast, EAM and MEAM show substantially larger deviations for certain components, exceeding 15–40% in some cases. For Cr (bcc), the present MTP significantly reduces the large errors observed in classical potentials. The relative error in C_{12}, which exceeds 100% for EAM and remains above 50% for MEAM, is reduced to below 2% in the present MTP. Similarly, shear components are predicted within approximately 5% deviation from DFT. In Fe (bcc), where magnetic effects strongly influence elastic response, the present MTP maintains deviations below approximately 10% for all elastic components. This represents a substantial improvement over EAM, which underestimates C_{11} by more than 30% and overestimates C_{44} by more than 50%. For Ni (fcc), the present MTP achieves relative errors below 5% for C_{11} and C_{12}, while the deviation in C_{44} remains below 12%, comparable to or smaller than those of EAM and MEAM.

When compared to the MTP-Cao model trained exclusively on ternary CoCrNi configurations, the present MTP demonstrates consistently lower relative errors for Cr and Fe elastic constants. This improvement highlights the importance of explicitly incorporating unary structures and multiphase configurations into the training database. The present MTP systematically improves upon classical EAM and MEAM potentials and enhances transferability relative to a ternary trained MTP. Accurate reproduction of unary elastic properties is critical for ensuring reliable predictions of defect energetics, stacking fault behavior, and composition-dependent mechanical response in the multicomponent alloy system.

2. Surface and defect properties

Surface energies and vacancy formation energies provide stringent tests of transferability because they probe low coordination environments and broken bond configurations that are not explicitly present in ideal bulk crystals. Accurate reproduction of these quantities is essential for reliable modeling of defect thermodynamics, diffusion processes, crack propagation, and radiation damage phenomena in multicomponent alloys. The present MTP reproduces vacancy formation energies of Co (hcp), Co (fcc), Cr (bcc), and Ni (fcc) within approximately 1–16% deviation as shown in Table II. In particular, the Cr (bcc) vacancy energy shows excellent agreement, with an error below 2%, whereas EAM and MEAM underestimate this quantity by 17–24%. For Co (fcc), the present MTP reduces the deviation to below 1%, outperforming both classical potentials and MTP-Cao. For Ni (fcc), the present MTP predicts the vacancy formation energy within approximately 2% of DFT, significantly improving upon EAM, which overestimates the value by nearly 50%. MEAM exhibits moderate deviation (∼15%), while MTP-Cao performs comparably but slightly less accurately than the present model. The largest deviation for the present MTP is observed in Fe (bcc), where the vacancy formation energy is underestimated by approximately 36%. This discrepancy is likely associated with the magnetic sensitivity of Fe and the complexity of vacancy induced local magnetic rearrangements.

Surface energies probe broken bonds and anisotropic bonding environments. Table II shows for Co (hcp) {0001}, the present MTP reproduces DFT within 1%, outperforming MEAM and matching or exceeding EAM accuracy. For Co (fcc) surfaces, deviations remain within 4–7% for the {100} and {111} facets. For Cr (bcc), the present MTP predicts the {100} surface energy within 0.3% of DFT, demonstrating near quantitative agreement, while EAM underestimates by 5% and MEAM by more than 30%. Similar trends are observed for other Cr facets, where classical potentials systematically underestimate surface energies. In Fe (bcc), the present MTP maintains errors within 1–6% across the {100}, {110}, and {112} surfaces. In contrast, EAM exhibits severe inconsistencies, including unphysical negative values for the {112} surface, highlighting limitations of empirical functional forms in highly anisotropic environments. For Ni (fcc), the present MTP predicts surface energies within approximately 6–16% of DFT. While deviations are slightly larger for certain facets, they remain systematically smaller than those of MEAM and comparable to or better than EAM.

3. Force validation

Figure 1 presents parity plots comparing DFT force magnitudes with those predicted by the present MTP for unary Co, Cr, Fe, and Ni configurations spanning strained,

TABLE I. Unary structural, elastic, and energetic properties of Co, Cr, Fe, and Ni predicted by different interatomic potentials compared with DFT.

Property	Expt.	DFT	EAM	MEAM	MTP-Cao	MTP-present
			Co (hcp)			
E_{coh} (eV/atom)	4.39 [68]		5.78	4.41	3.58	4.10
a (Å)	2.51 [69]	2.49	2.50	2.50	2.50	2.49
c (Å)	4.07 [69]	4.03	4.06	4.08	4.00	4.03
C_{11} (GPa)	293 [70]	364	344	322	383	383
C_{12} (GPa)	142 [70]	175	192	140	158	176
C_{13} (GPa)	90 [70]	119	195	123	94	118
C_{33} (GPa)	339 [70]	403	357	339	318	384
C_{44} (GPa)	78 [70]	95	61	69	77	79
$\Delta E_{hcp-fcc}$ (eV)		0.014	−0.014	0.004	0.015	0.014
$\Delta E_{hcp-bcc}$ (eV)		0.082	0.108	0.047	0.096	0.062
$\Delta E_{hcp-\omega}$ (eV)		0.082	0.082	0.106	0.108	0.080
ΔE_{hcp-SC} (eV)		0.760	0.583	0.668	0.706	0.760
			Co (fcc)			
a (Å)	3.54 [71]	3.52	3.52	3.54	3.53	3.49
C_{11} (GPa)	260 [72]	325	282	280	296	301
C_{12} (GPa)	160 [72]	189	174	152	165	180
C_{44} (GPa)	110 [72]	156	105	110	159	154
			Cr (bcc)			
E_{coh} (eV/atom)	4.10 [73]		6.02	4.10	3.94	4.05
a (Å)	2.88 [73]	2.86	2.89	2.88	2.85	2.87
C_{11} (GPa)	410.7 [73]	434	383	344	553	451
C_{12} (GPa)	106.7 [73]	73	182	113	380	72
C_{44} (GPa)	105 [73]	119	91	130	67	121
$\Delta E_{bcc-fcc}$ (eV)		0.390	4.315	4.187	0.109	0.358
$\Delta E_{bcc-hcp}$ (eV)		0.404	4.321	4.159	0.107	0.347
$\Delta E_{bcc-a15}$ (eV)		0.084	4.145	4.143	0.104	0.299
ΔE_{bcc-SC} (eV)		1.019	5.002	5.191	0.701	0.784
			Fe (bcc)			
E_{coh} (eV/atom)	4.28 [68]		4.30	4.29		4.27
a (Å)	2.86 [74]	2.83	2.86	2.86		2.84
C_{11} (GPa)	240 [75]	274	185	242		280
C_{12} (GPa)	136 [75]	143	187	138		158
C_{44} (GPa)	120 [75]	103	165	121		121
$\Delta E_{bcc-fcc}$ (eV)		0.142	−0.099	0.048		0.115
$\Delta E_{bcc-hcp}$ (eV)		0.084	−0.093	0.029		0.158
$\Delta E_{bcc-a15}$ (eV)		0.089	0.139	0.027		0.152
ΔE_{bcc-SC} (eV)		0.755	0.763	0.984		0.628
			Ni (fcc)			
E_{coh} (eV/atom)	4.44 [68]		3.33	4.45	2.74	4.52
a (Å)	3.51 [76]	3.52	3.52	3.52	3.51	3.52
C_{11} (GPa)	261.2 [77]	276	261	261	254	268
C_{12} (GPa)	150.8 [77]	161	155	151	164	161
C_{44} (GPa)	131.7 [77]	127	123	132	107	113
$\Delta E_{fcc-bcc}$ (eV)		0.095	0.089	0.088	0.048	0.093
$\Delta E_{fcc-hcp}$ (eV)		1.379	0.027	0.021	–0.007	0.030
$\Delta E_{fcc-a15}$ (eV)		0.133	0.105	0.246	0.107	0.140
ΔE_{fcc-SC} (eV)		0.692	0.714	0.664	0.692	0.550

perturbed, and surface environments. For Co, the MTP achieves an root mean square error (RMSE) of 0.051 eV/Å with a correlation coefficient $R = 0.999$, indicating perfect agreement across the sampled force range. Similarly, Ni exhibits an RMSE of 0.044 eV/Å and $R = 1.000$, demonstrating excellent consistency between MTP and DFT forces. For Cr, the RMSE increases to 0.100 eV/Å with $R = 0.993$, yet the parity distribution remains tightly clustered along the ideal diagonal, indicating robust force prediction even in highly distorted configurations. Fe shows the largest

TABLE II. Vacancy formation energies (eV) and surface energies (mJ/m^2) calculated using DFT and various interatomic potentials.

	DFT	EAM	MEAM	MTP-Cao	MTP-present
			Vacancy formation energy (eV)		
Co(hcp)	1.90	1.49	1.46	1.64	1.60
Co(fcc)	1.71	1.54	1.45	1.60	1.72
Cr(bcc)	2.64	2.00	2.18	2.08	2.61
Fe(bcc)	2.20	1.80	1.70		1.40
Ni(fcc)	1.31	1.93	1.51	1.37	1.29
			Surface energy (mJ/m^2)		
Co(hcp) {0001}	2099	2007	1933	2189	2079
Co(hcp) {10$\bar{1}$0}	2259	2876	2427	2402	2825
Co(fcc) {100}	2451	2442	2106	1892	2345
Co(fcc) {110}	2403	2539	2086	1983	2524
Co(fcc) {111}	2067	2248	1922	1655	2104
Cr(bcc) {100}	3370	3189	2354	2575	3379
Cr(bcc) {110}	3440	2908	2289	2378	3188
Cr(bcc) {112}	—	3159	2399	2630	3430
Fe(bcc) {100}	2435	1978	2506		2462
Fe(bcc) {110}	2370	1326	2350		2414
Fe(bcc) {112}	2697	−3354	2461		2527
Ni(fcc) {100}	2239	2227	1936	1763	2378
Ni(fcc) {110}	2343	2679	2227	1865	2482
Ni(fcc) {111}	1919	2056	1599	1567	2227

DFT vacancy formation energies: Co(fcc) [78], Co(bcc) [79], Co(hcp) [80], Fe(bcc) [81], Ni(fcc) [82]. DFT surface energies: Co(hcp) and Co(fcc) [83], Cr(bcc) [84], Fe(bcc) [85], Ni(fcc) [82].

deviation, with an RMSE of 0.312 eV/Å and $R = 0.969$. The broader scatter observed for Fe likely reflects the sensitivity of Fe (bcc) to magnetic effects and the complexity of force responses in strained and perturbed environments. Nevertheless, the correlation remains high, and no systematic bias is observed. Across all elements, the force predictions exhibit strong linearity and minimal systematic deviation, confirming that the MTP accurately captures local energy gradients. The high correlation coefficients ($R > 0.96$ for all cases) demonstrate that the model maintains consistency across a wide force spectrum, including low force near equilibrium configurations and high force distorted states.

4. Phonon dispersion

Phonon dispersion relations provide a stringent test of dynamical stability and the curvature of the potential energy surface around equilibrium configurations. Unlike elastic constants, which probe only long-wavelength acoustic modes, phonon spectra assess both acoustic and optical branches across the Brillouin zone. Accurate reproduction of phonon frequencies therefore indicates that the potential correctly captures second-order force constants and interatomic bonding stiffness. Figure 2 compares phonon dispersion curves obtained from DFT and the present MTP for Co (hcp) Co (fcc), Fe (bcc), and Ni (fcc). For Co (hcp) and Co (fcc), the MTP reproduces both acoustic and optical branches with excellent agreement across high symmetry directions. The slopes near the Γ point, which are directly related to elastic constants, are well captured, consistent with the previously discussed elastic validation. No spurious imaginary modes are observed, confirming dynamical stability. In Fe (bcc), the overall dispersion trends are accurately reproduced, particularly for the transverse acoustic branches along the Γ–H and Γ–N directions. Minor deviations appear at higher frequencies, yet the qualitative band structure and branch ordering remain consistent with DFT results. For Ni (fcc), the MTP closely follows DFT phonon frequencies throughout the Brillouin zone. The acoustic branches and high frequency longitudinal modes are well described, with only small shifts in optical like features at the zone boundaries.

Elemental Cr adopts an AFM ground state, which doubles the primitive bcc unit cell and introduces additional folded phonon branches relative to the one atom bcc structure. Because the present MTP does not explicitly include magnetic degrees of freedom, direct comparison with antiferromagnetic phonon dispersion would not constitute a strictly equivalent reference. Although spin polarization is accounted for in the DFT training data, the potential itself represents a nonmagnetic energy surface. For this reason, Cr phonon dispersion is not included in the direct comparison.

5. Stacking fault energy

The generalized stacking fault energy (GSFE) surface provides critical insight into dislocation core structure, partial dislocation separation, and deformation mechanisms. Accurate reproduction of unstable stacking fault energies (γ_{usf}) and intrinsic stacking fault energies (γ_{isf}) is essential for modeling slip behavior, twinning propensity, and plastic anisotropy in multicomponent alloys. Figure 3 compares GSFE curves obtained from DFT and various interatomic potentials for representative slip systems in Co, Cr, Fe, and Ni. For Co

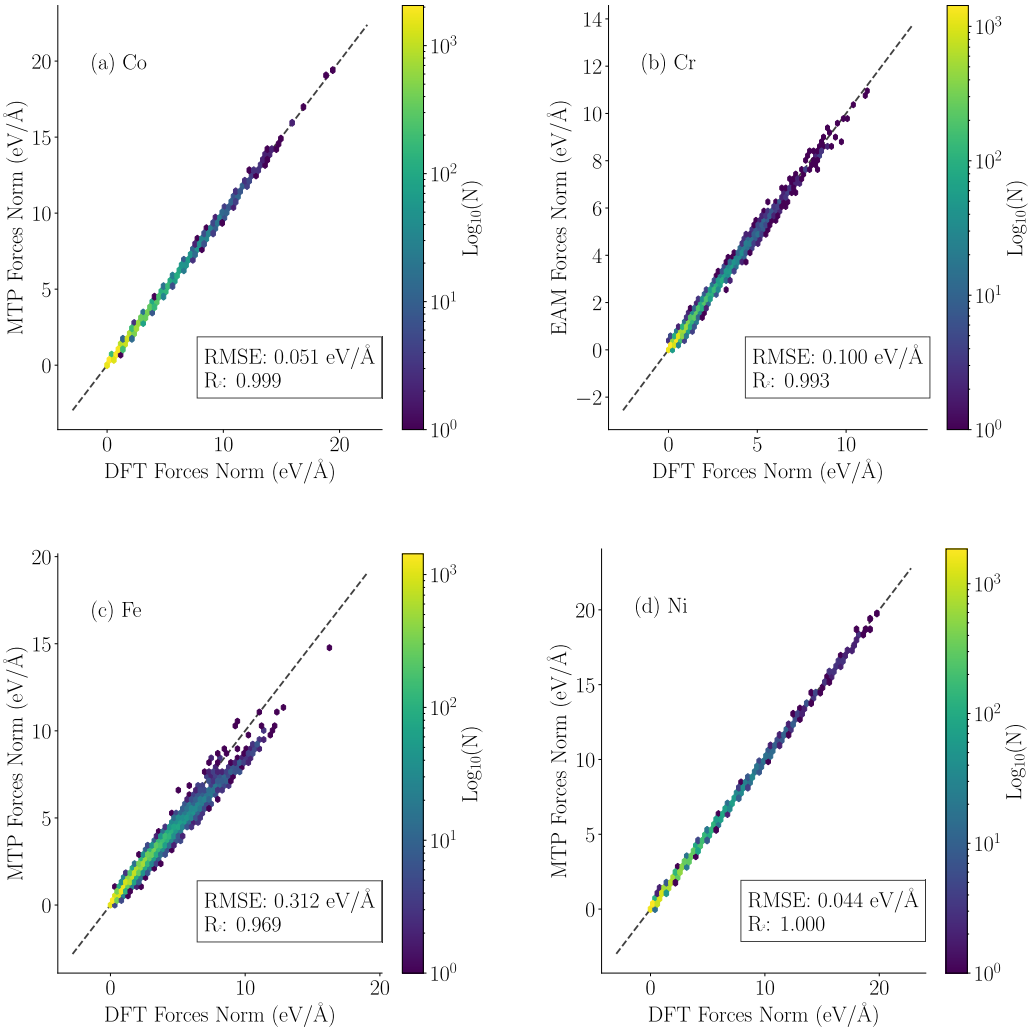

FIG. 1. Parity plots comparing DFT and MTP predicted force magnitudes for unary (a) Co, (b) Cr, (c) Fe, and (d) Ni configurations. Each point represents an atomic force component from strained, thermally perturbed, and surface structures included in the dataset. The dashed line denotes perfect agreement. The color scale indicates the logarithm of the number of data points [$\log_{10}(N)$]. RMSE and R are reported for each element.

(hcp) along the $\langle 11\bar{2}0\rangle$ direction on the (0001) plane, the present MTP closely reproduces both the unstable stacking fault maximum and the intrinsic fault minimum, with peak energies within approximately 5–8% of DFT values. In contrast, EAM underestimates the unstable peak, while MEAM slightly overestimates the overall barrier height. MTP-Cao shows moderate deviation in the intrinsic fault region. For Co (fcc) on the {111} plane along $\langle 11\bar{2}\rangle$, the MTP captures the characteristic double hump profile of the GSFE curve and predicts the unstable stacking fault energy within approximately 5% of DFT. Classical potentials exhibit larger deviations, particularly in the fault minimum region, indicating limited accuracy in describing partial dislocation energetics. In Cr (bcc) and Fe (bcc) along the $\{110\}\langle 111\rangle$ slip system, the present MTP reproduces the overall barrier shape and peak magnitude with good agreement to DFT. For Cr, the unstable stacking fault energy is predicted within roughly 10% deviation, while EAM and MEAM systematically underestimate the barrier. For Fe, the MTP captures the barrier height and symmetry of the curve, whereas EAM significantly underestimates the entire energy landscape, indicating poor representation of shear resistance. For Ni (fcc) on the {111} plane, the present MTP accurately reproduces both γ_{usf} and γ_{isf} values, with deviations generally below 10%. MEAM and EAM overestimate the unstable barrier. It is important to note that the MTP-Cao potential predicts a negative energy difference between fcc and hcp Ni ($\Delta E_{\text{fcc-hcp}} = -0.007\,\text{eV}$), implying that hcp Ni is energetically favored over the experimentally stable fcc phase. This incorrect phase ordering leads directly to negative intrinsic stacking fault energies for Ni.

6. Decohesion energy

Decohesion energy curves describe the nonlinear response of interatomic bonding under tensile separation and provide insight into surface formation, cleavage behavior, and fracture resistance. Figure 4 compares decohesion energy curves obtained from DFT and various interatomic potentials for representative crystallographic planes of Co, Cr, Fe, and Ni. For Co (hcp) (0001), the present MTP closely follows

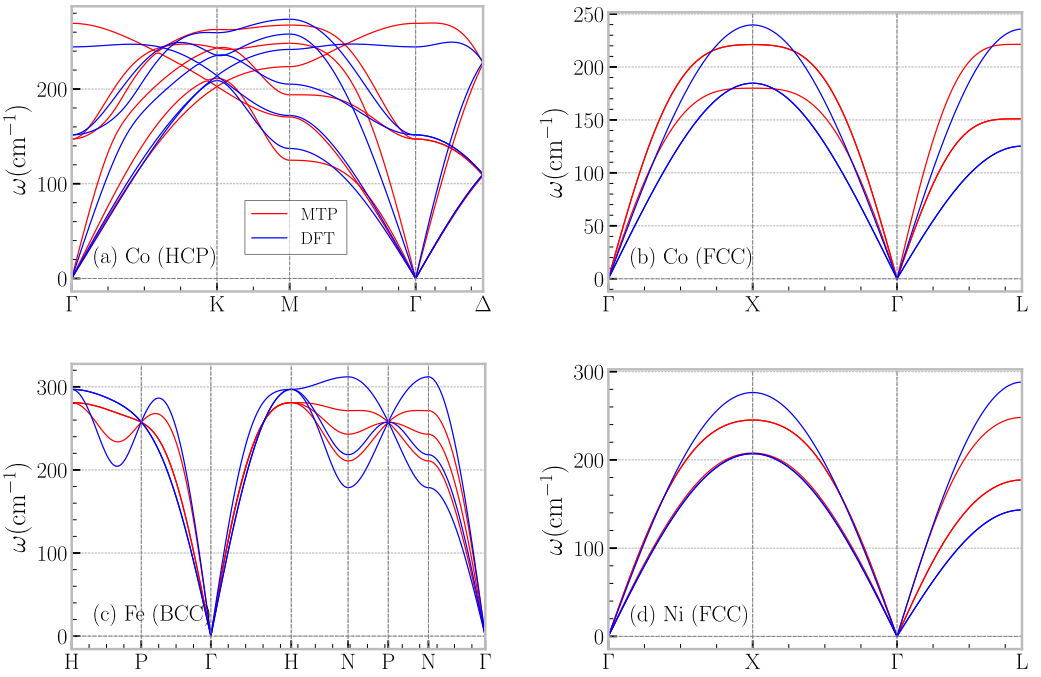

FIG. 2. Phonon dispersion relations calculated using DFT (blue) and the present MTP (red) for (a) Co (hcp), (b) Co (fcc), (c) Fe (bcc), and (d) Ni (fcc) along high-symmetry directions of the Brillouin zone.

the DFT curve across the entire separation range. The peak cleavage energy and asymptotic surface formation energy are reproduced within approximately 5% deviation. In contrast, MEAM underestimates the maximum separation energy and exhibits a discontinuity near intermediate separation, while MTP-Cao underpredicts the final cleavage plateau. For Cr (bcc) (110), the MTP accurately captures both the curvature and maximum decohesion energy, remaining within approximately 5–8% of DFT throughout the separation process. EAM slightly underestimates the peak energy, whereas MEAM significantly underpredicts the entire curve and exhibits non-physical slope changes at intermediate separations. In Fe (bcc) (110), the present MTP reproduces the overall shape and peak magnitude of the decohesion curve with good agreement to DFT. EAM substantially underestimates the cleavage energy and fails to capture the correct asymptotic behavior, while MEAM exhibits abrupt slope variations indicative of limited transferability in bond-breaking regimes. For Ni (fcc) (111), the MTP maintains close agreement with DFT for both the rising tensile region and the final separation plateau. Classical potentials show larger deviations, particularly in the intermediate separation region where bond breaking initiates.

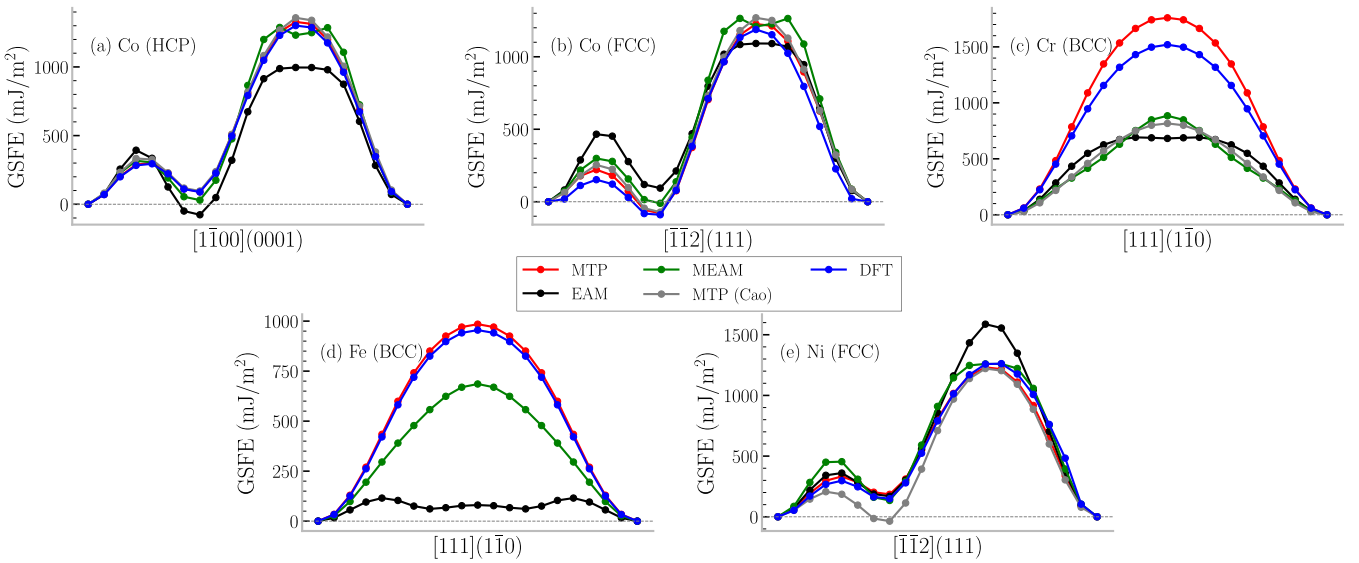

FIG. 3. GSFE curves calculated using DFT and various interatomic potentials for representative slip systems in (a) Co (hcp), (b) Co (fcc), (c) Cr (bcc), (d) Fe (bcc), and (e) Ni (fcc).

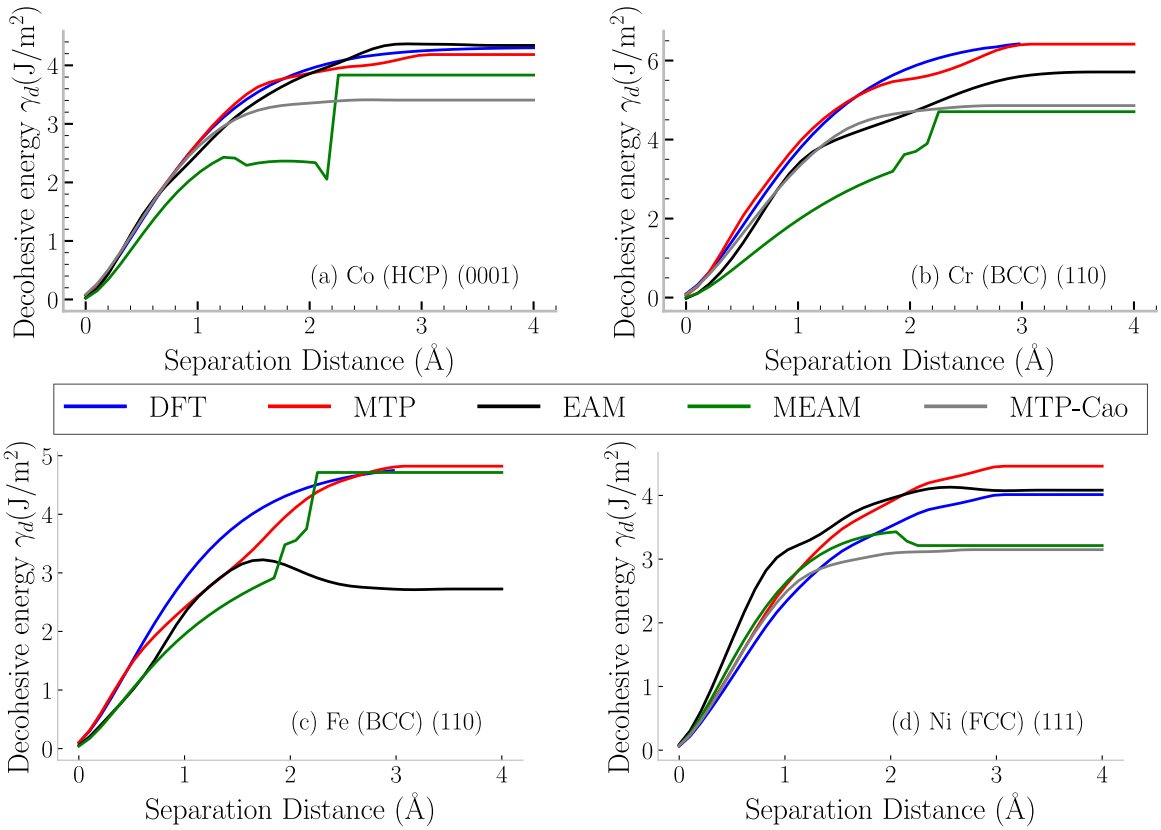

FIG. 4. Decohesion energy as a function of interplanar separation for (a) Co (hcp) (0001), (b) Cr (bcc) (110), (c) Fe (bcc) (110), and (d) Ni (fcc) (111), comparing DFT and various interatomic potentials. The present MTP reproduces both the peak cleavage energy and asymptotic surface formation energy with high fidelity.

B. Binary elements

1. Substitutional energies

Unrelaxed substitutional energies provide a direct measure of chemical affinity in dilute limits and offer a complementary perspective to the CSRO analysis. As shown in Table III, DFT predicts strong attractive interactions between Co and Ni, as well as Fe and Ni, while Cr generally exhibits weaker or slightly repulsive behavior in Ni and Co hosts. The present MTP successfully reproduces the qualitative sign structure of these interactions across all examined host solute pairs. In particular, the favorable Fe-in-Ni substitution energy and the weakly repulsive Cr-in-Ni tendency are captured with correct sign and comparable magnitude. Although the absolute magnitudes are somewhat reduced relative to DFT, the chemical hierarchy among Co–Ni, Fe–Ni, and Cr–Ni interactions is preserved. In contrast, classical EAM and MEAM potentials exhibit multiple sign reversals and large quantitative deviations. For example, EAM predicts strongly attractive Cr-in-Ni interactions and unfavorable Ni-in-Co substitution, both inconsistent with DFT. Such inaccuracies in dilute chemical energetics can propagate into incorrect predictions of mixing enthalpy and short range ordering. The improved consistency of the present MTP reflects the importance of explicitly including unary, binary, and multicomponent configurations in the training database, thereby constraining local chemical energetics in a physically meaningful manner.

TABLE III. Unrelaxed substitutional energies (eV) for single atom substitutions among Co, Cr, Fe, and Ni in their stable crystal structures, predicted by different interatomic potentials compared with DFT.

Substitution	DFT	EAM	MEAM	MTP-Cao	MTP
			Co (hcp)		
Cr	0.18	–0.14	0.36	0.35	0.38
Fe	0.09	1.10	–0.002		0.15
Ni	–0.07	1.08	0.09	0.06	–0.02
			Cr (bcc)		
Co	0.28	1.00	1.47	0.23	0.50
Fe	0.92	–1.18	0.70		1.03
Ni	0.52	1.27	0.57	0.27	0.60
			Fe (bcc)		
Co	0.22	0.46	0.12		0.29
Cr	0.18	0.25	0.76		0.22
Ni	0.21	0.43	0.30		0.20
			Ni (fcc)		
Co	–0.03	0.18	–0.031	0.11	–0.005
Cr	0.07	–0.45	0.09	–0.22	–0.06
Fe	–0.42	–0.003	–0.05		–0.26

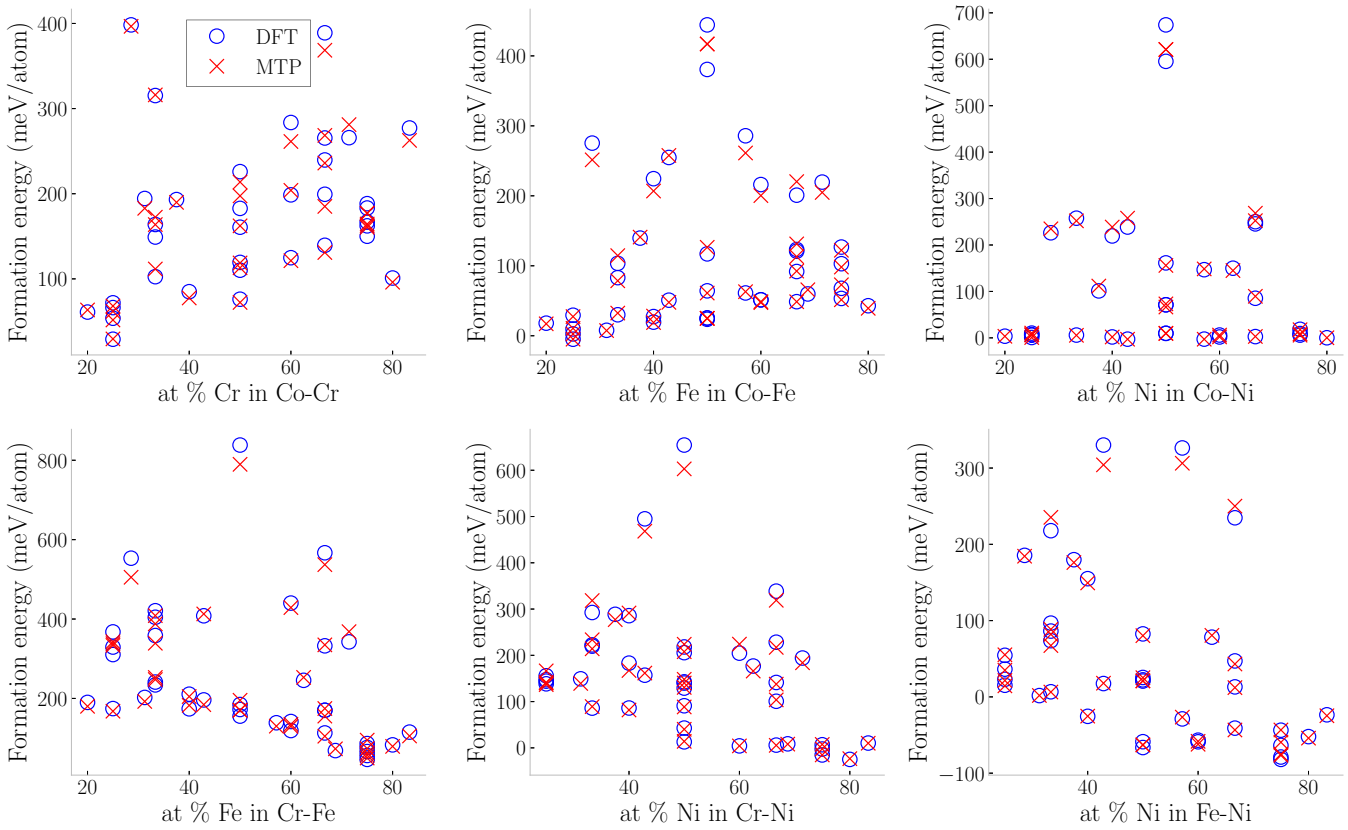

FIG. 5. Binary formation energies as a function of composition for all elemental pairs in the Co–Cr–Fe–Ni system, comparing DFT and MTP predictions.

2. *Convexhull*

To further assess the thermodynamic consistency of the developed MTP, binary formation energies were evaluated across the full composition range for all elemental pairs, as shown in Fig. 5. The MTP predictions closely follow DFT results for Co–Cr, Co–Fe, Co–Ni, Cr–Fe, Cr–Ni, and Fe–Ni systems. The overall curvature of the formation energy landscape, which governs phase stability and mixing behavior, is accurately reproduced. Importantly, no artificial stabilization of spurious intermetallic compounds is observed, and the convexity of the formation energy curves remains consistent with DFT. While slight deviations appear at higher formation energies, particularly for strongly unstable configurations, the relative energetic ordering and near hull behavior are preserved. This agreement confirms that the MTP captures the essential thermodynamic driving forces for chemical mixing and segregation across the binary subsystems.

C. Trinary and quaternary elements

1. *Force validation*

The fidelity of the MTP was assessed by comparing predicted atomic forces with DFT references for the ternary CoCrNi and quaternary CoCrFeNi datasets (Fig. 6). Figures 6(a) and 6(d) show parity plots of force norms, with points tightly clustered along the diagonal [color indicates $\log_{10}(N)$)] yielding RMSEs of 0.153 eV/Å (CoCrNi) and 0.203 eV/Å (CoCrFeNi) with $R^2 = 0.996$–0.997. Componentwise errors are similarly low: For CoCrNi, $\mathrm{RMSE}_{x,y,z} = \{0.146, 0.145, 0.145\}$ eV/Å with $R^2 = 0.995$ for each; for CoCrFeNi, $\mathrm{RMSE}_{x,y,z} = \{0.186, 0.184, 0.184\}$ eV/Å with $R^2 = 0.996$. Figures 6(b) and 6(e) plot the difference in magnitudes, $\Delta = |\mathbf{f}_{\mathrm{MTP}}| - |\mathbf{f}_{\mathrm{DFT}}|$, versus $|\mathbf{f}_{\mathrm{DFT}}|$; the distributions are narrowly centered around zero, with mean $|\Delta| = 0.112$ (median 0.083) eV/Å and mean relative $|\Delta| = 8.61\%$ for CoCrNi, and mean $|\Delta| = 0.139$ (median 0.095) eV/Å and mean relative $|\Delta| = 9.17\%$ for CoCrFeNi. Figures 6(c) and 6(f) report the angle between the DFT and MTP force vectors; the orientations are strongly aligned, with mean (median) angles of 7.78° (4.54°) for CoCrNi and 7.82° (4.13°) for CoCrFeNi, and 95th percentiles of 25.13° and 27.20°, respectively. The close agreement between predicted and reference forces confirms the reliability of the trained MTP in capturing atomic-scale interactions, which is essential for accurate modeling of mechanical behavior, defect energetics, and diffusion mechanisms in these two MEAs.

2. *Elastic properties*

To ensure that the atomic structures represent the lowest energy configurations, a $10 \times 10 \times 10$ supercell constructed from a four-atom fcc unit cell was used (4000 atoms). First, an equiatomic-composition supercell was constructed; it followed that hybrid Monte Carlo (MC)/MD simulations [86] were performed at 300 K, where MC trial swaps explore configurational space while MD relaxations minimize atomic forces and stresses. This approach allows for efficient

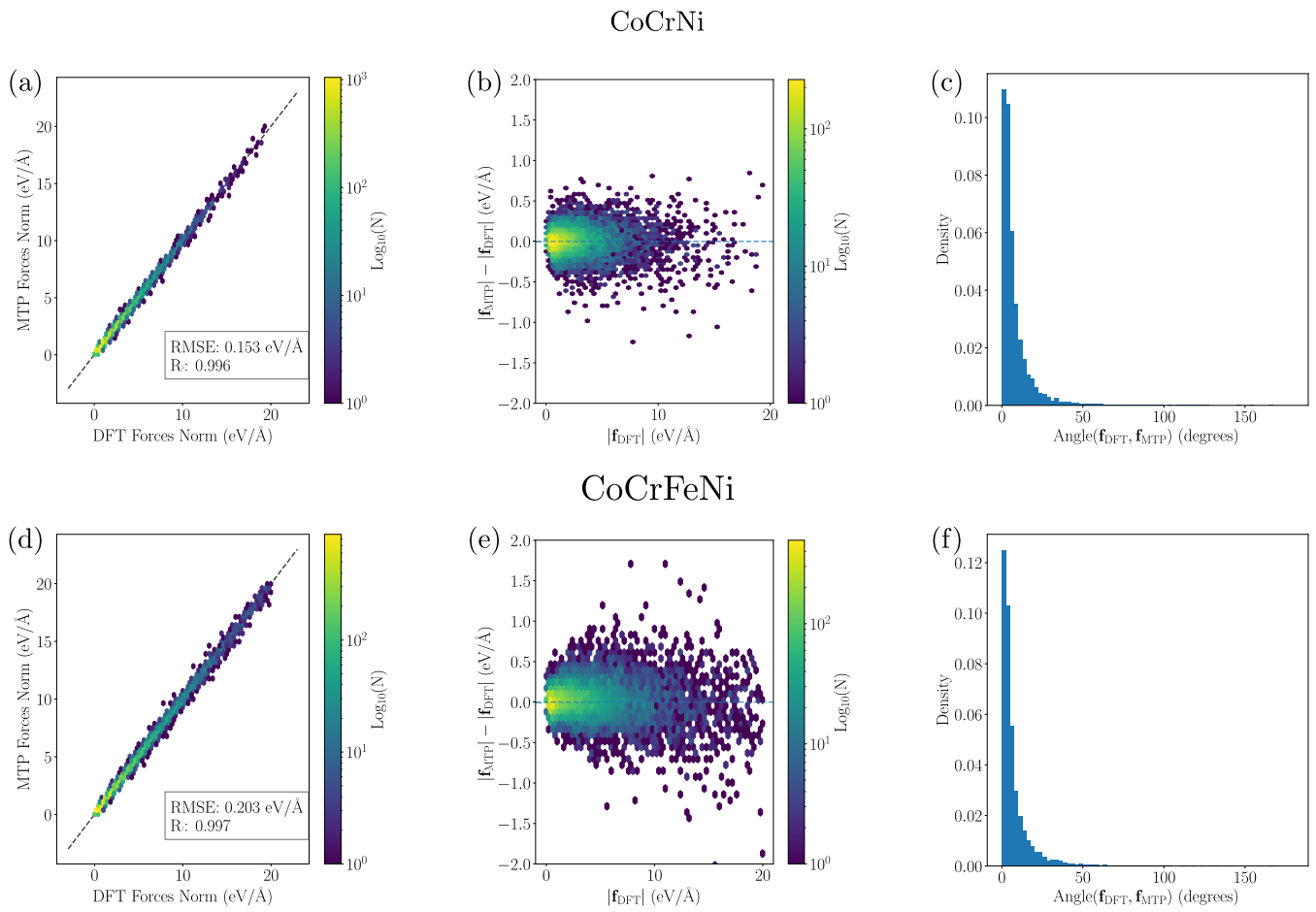

FIG. 6. Force validation of the MTP against DFT for CoCrNi (a)–(c) and CoCrFeNi (d)–(f). (a), (d) Parity plots of force norms $|\mathbf{f}|$ shown as hexbin density maps (color indicates $\log_{10}(N)$) exhibit tight clustering along the diagonal. (b,e) The magnitude deviation $\Delta = |\mathbf{f}_{\mathrm{MTP}}| - |\mathbf{f}_{\mathrm{DFT}}|$ versus $|\mathbf{f}_{\mathrm{DFT}}|$ is narrowly centered around zero across the dataset. (c), (f) Distributions of the angle between $\mathbf{f}_{\mathrm{DFT}}$ and $\mathbf{f}_{\mathrm{MTP}}$ are concentrated at small values, indicating strong directional agreement.

convergence toward minimum-energy configurations by combining compositional and positional optimization. The hybrid simulations were conducted for 5 000 000 steps, with an energy convergence criterion requiring that the change in total energy after each MC cycle be less than 1×10^{-6} eV/atom, following the methodology outlined by [87]. The resulting atomic arrangements were then relaxed into low-energy states, naturally incorporating CSRO effects as a consequence of energy minimization, consistent with previous findings for CoCrFeNi-based alloys [88–90]. The elastic constants of CoCrNi and CoCrFeNi obtained from MTP, EAM, MEAM, DFT, and experiment are summarized in Table IV. For both alloys, the lattice constants predicted by all methods lie within the narrow range of 3.53–3.56 Å, in acceptable agreement with experimental measurements, confirming that the fcc structure is well captured across approaches.

In terms of elastic response, the MTP predictions are in closest agreement with DFT and experimental data. For CoCrNi, MTP yields $C_{11} = 245$ GPa, $C_{12} = 152$ GPa, and $C_{44} = 148$ GPa, values nearly identical to the experimental measurements of $C_{11} = 249$ GPa, $C_{12} = 156$ GPa, and $C_{44} = 142$ GPa. Similarly, for CoCrFeNi, MTP reproduces the balance among C_{11}, C_{12}, and C_{44} within the DFT range, further confirming its fidelity. In contrast, EAM and MEAM systematically underestimate the shear modulus C_{44} (e.g., $C_{44} = 95$ GPa and 82 GPa in CoCrNi), while slightly overestimating C_{12}, leading to an overprediction of the bulk modulus B. These deficiencies reflect their empirical nature and lack of explicit electronic structure and magnetic contributions.

3. Optimal solid-solution prediction

To evaluate the predictive capability of the developed MTP beyond its training composition, we investigated the mechanical response of nonequiatomic CoCrFeNi alloys using hybrid MC/MD simulations followed by elastic tensor evaluation. Importantly, the MTP was trained exclusively on equiatomic CSRO configurations, and no nonequiatomic compositions were included in the fitting database. The following results therefore constitute a genuine transferability test across composition space rather than interpolation within the training manifold. Bulk modulus (B_0) and shear modulus (G_0) were computed from MTP-relaxed structures and compared to DFT results obtained for the same compositions and equivalent configurational sampling [31]. Figures 7 and 8 present the composition–property maps across a representative subset of nonequiatomic alloys. Despite the restricted training domain, the MTP reproduces the DFT ordering of the softest and

TABLE IV. Comparison of elastic constants C_{ij} (GPa) and lattice constant a (Å) of two equiatomic MEAs obtained from MTP, EAM, MEAM, special quasirandom structures (SQS) from DFT, and experiment. Percent errors in parentheses are relative to DFT.

Alloy	Method	a (Å)	C_{11}	C_{12}	C_{44}	B
CoCrFeNi	MTP (SQS)	3.55 (−0.3%)	214 (−10.1%)	138 (−14.8%)	136 (−21.4%)	164 (−21.9%)
	MTP (SRO)	3.55 (−0.3%)	246 (+3.4%)	139 (−14.2%)	149 (−13.9%)	175 (−16.7%)
	MEAM [35]	3.54 (−0.6%)	240 (+0.8%)	166 (+2.5%)	80 (−53.8%)	190 (−9.5%)
	DFT [91]	3.56	238	162	173	210
	Expt [92]		238	151	168	182
CoCrNi	MTP (SQS)	3.54 (+0.3%)	247 (−7.5%)	149 (−18.1%)	145 (−18.5%)	182 (−13.3%)
	MTP (SRO)	3.53 (0.0%)	266 (−0.4%)	145 (−20.3%)	155 (−12.9%)	186 (−11.4%)
	MTP-Cao (SQS)	3.52 (−0.3%)	300 (+12.4%)	189 (+3.8%)	153 (−14.0%)	226 (+7.6%)
	MTP-Cao (SRO)	3.52 (−0.3%)	309 (+15.7%)	196 (+7.7%)	156 (−12.4%)	234 (+11.4%)
	EAM	3.56 (+0.8%)	252 (−5.6%)	178 (−2.2%)	95 (−46.6%)	203 (−3.3%)
	MEAM	3.54 (+0.3%)	248 (−7.1%)	166 (−8.8%)	82 (−53.9%)	192 (−8.6%)
	DFT [91]	3.53	267	182	178	210
	Expt (298K) [93]	3.56	249	159	138	189
	Expt (fit) [93]		255	159	146	191

stiffest compositions. Consistent with first principles trends, Fe enrichment systematically lowers B_0, whereas Co enrichment increases G_0. Specifically, the three lowest B_0 compositions all contain 40% Fe, while the highest B_0 compositions are Fe-lean (10%). Similarly, the lowest G_0 alloys are characterized by low Co (10%) and high Cr (40%), whereas the highest G_0 alloys exhibit high Co (40%) combined with low Ni (10%). The results are summarized in Tables V and VI.

While absolute deviations reach up to approximately 40 GPa for specific compositions (Table V), the dominant compositional trends and ranking of extremal alloys are preserved. This indicates that the MTP correctly captures the underlying chemical stiffness hierarchy governed by electronic structure effects, even outside the equiatomic training point. These findings are consistent with earlier EMTO-CPA first principles studies [31] which identified Fe as the primary

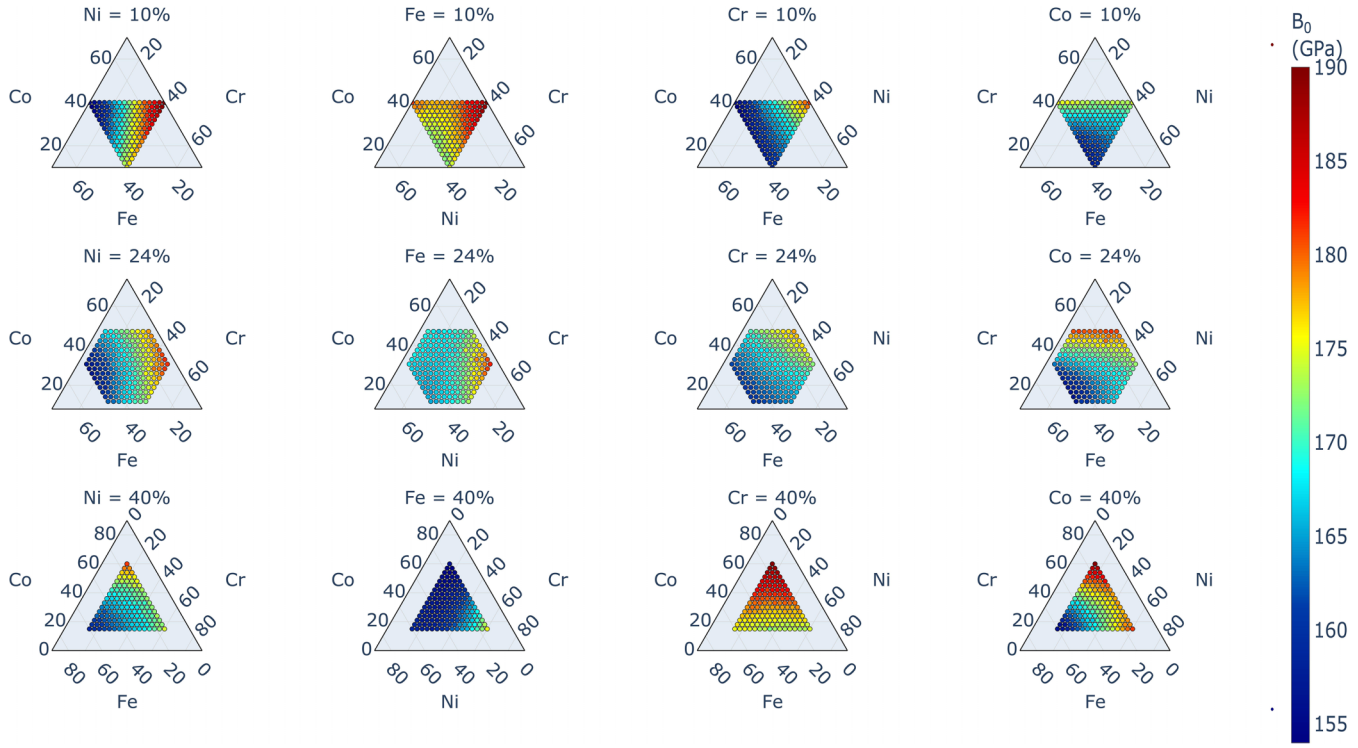

FIG. 7. Predicted bulk modulus, B_0 (GPa), for nonequiatomic CoCrFeNi alloys obtained from MTP after MC/MD relaxation of CSRO configurations. Each cell in the grid corresponds to a unique composition (ordered as Co, Cr, Fe, Ni) and is colored by the resulting B_0; darker/lighter shades indicate lower/higher stiffness, respectively. The map reveals smooth, physically consistent trends across composition space: Fe enrichment is associated with reduced B_0 (a low-B_0 corridor in Fe-rich regions), while Fe-lean compositions exhibit higher B_0. The ordering of the lowest and highest B_0 compositions matches DFT at the same compositions, as summarized in Table V, supporting the transferability of the model beyond its training point.

TABLE V. Top three alloys (Co, Cr, Fe, Ni %) with the lowest and highest bulk modulus values (B_0 in GPa) as calculated by MTP and DFT. The MTP predictions show good agreement with DFT results, confirming that Fe has the most significant influence on B_0: increasing Fe content (e.g., 10% → 40%) corresponds to a decrease in B_0.

Low B_0				High B_0			
MTP	B_0	DFT	B_0	MTP	B_0	DFT	B_0
38, 12, 40, 10	154	10, 26, 40, 24	177	40, 40, 10, 10	190	40, 40, 10, 10	232
38, 10, 40, 12	154	34, 16, 40, 10	177	38, 40, 10, 12	189	38, 40, 10, 12	231
36, 12, 40, 12	155	12, 26, 40, 22	178	38, 40, 10, 12	188	40, 38, 10, 12	231

softening element and Co as the dominant shear-stiffening component. The ability of the present MTP to reproduce these trends across quaternary composition space demonstrates that the potential can be used as an efficient screening tool for identifying mechanically optimal solid-solution chemistries, enabling large scale exploration beyond the reach of DFT.

4. Short-range ordering

CSRO in MEAs is increasingly recognized as a critical structural feature that governs their thermodynamic stability and mechanical performance [90,94,95]. Contrary to the idealized view of MEAs as random solid solutions, recent computational and experimental evidence highlights that local chemical ordering, particularly at low temperatures, can significantly affect stacking fault energies, magnetic configurations, lattice distortions, and melting points [89]. CSRO introduces preferential pairwise interactions between atoms, which modify the local atomic environments and reduce configurational entropy, ultimately stabilizing certain atomic configurations. In alloys like CoCrNi and CoCrFeNi, this ordering leads to the formation of chemically distinct domains, enhancing mechanical strength and resistance to deformation by increasing energy barriers for dislocation motion. Moreover, CSRO can influence the electronic density of states and magnetic interactions by modifying the overlap between atomic orbitals and altering the alignment of local magnetic moments, especially in elements like Cr that exhibit antiferromagnetic tendencies [60]

In the DFT-informed MC simulations by [60], strong CSRO was observed in both CoCrNi and CoCrFeNi alloys.

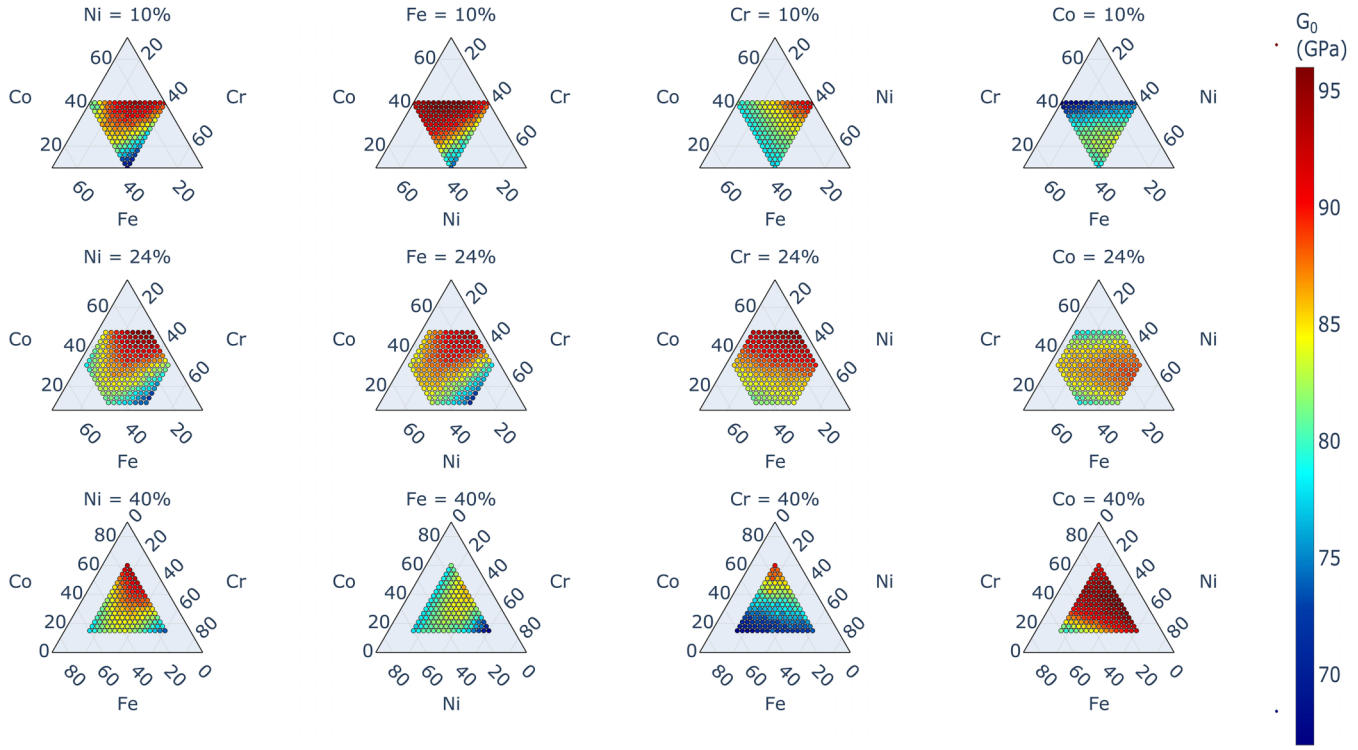

FIG. 8. Predicted shear modulus, G_0 (GPa), for nonequiatomic CoCrFeNi alloys obtained from MTP after MC/MD relaxation of CSRO configurations. The composition grid (ordered as Co, Cr, Fe, Ni) is colored by the resulting G_0, highlighting systematic trends in rigidity with chemistry. Co enrichment correlates with increased G_0 (high-G_0 band in Co-rich regions), whereas low-Co/high-Cr combinations tend to yield reduced G_0; compositions that are simultaneously Co-rich and Ni-lean are among the stiffest in shear. The MTP reproduces the DFT ranking of the lowest and highest G_0 compositions (Table VI), indicating that both models capture the dominant role of Co (and the secondary influence of Cr/Ni) in controlling shear rigidity across this quaternary space.

TABLE VI. Top three alloys (Co, Cr, Fe, Ni %) with the lowest and highest shear modulus values (G_0 in GPa) as calculated by MTP and DFT. The MTP predictions broadly track DFT trends; increasing Co content corresponds to an increase in G_0.

Low G_0				High G_0			
MTP	G_0	DFT	G_0	MTP	G_0	DFT	G_0
10, 40, 40, 10	67	10, 40, 16, 34	84	40, 28, 10, 22	96	40, 16, 34, 10	117
10, 40, 34, 16	68	10, 40, 18, 32	84	40, 24, 10, 26	96	40, 14, 36, 10	117
10, 40, 36, 14	68	10, 40, 14, 36	84	40, 18, 10, 32	96	40, 18, 32, 10	117

Cr–Cr and Fe–Fe pairings exhibited strong repulsion (positive Warren-Cowley parameters), while Ni–Cr and Ni–Fe demonstrated attractive ordering (negative values), indicating a strong preference for heterogeneous atomic pairs. This chemical ordering led to a significant reduction in formation energy and configurational entropy, reinforcing its thermodynamic significance. Notably, magnetic frustration emerged as a key consequence: the Cr sublattice exhibited antiferromagnetic ordering, influenced by the CSRO patterns, whereas other elements remained weakly magnetic. In contrast, results obtained using classical EAM potentials [56], analyzed by [87], showed qualitatively similar but quantitatively weaker CSRO trends. The CoCrNi system modeled with an EAM potential failed to capture the full extent of Cr–Cr repulsion and Ni–Cr affinity seen in DFT, largely due to the limitations of EAM in describing directional bonding and magnetic interactions. EAM relies on parameterized, empirical descriptions of atomic interactions, and lacks the quantum mechanical rigor needed to account for electronic structure effects and magnetism, explaining its reduced accuracy in predicting CSRO magnitudes and their consequences.

Although the MTP is not explicitly trained on spin moments, it is fitted to energy, force, and stress data from spin-polarized DFT calculations. Thus, it implicitly retains magnetic effects while remaining computationally efficient. To model CSRO, hybrid MD/MC simulations are performed in an isothermal–isobaric (NPT) ensemble at 500,800 and 1200 K until the system's energy converges. The Warren–Cowley parameter is used to quantify CSRO:

$$\alpha_{ij}^{n} = \frac{p_{ij}^{n} - c_j}{\delta_{ij} - c_j},$$

where n is the nth-nearest neighbor shell of a central atom of type i, p_{ij}^{n} the probability of finding a j-type atom in that shell, c_j the concentration of element j, and δ_{ij} the Kronecker delta. In a random alloy, $\alpha_{ij}^{n} \approx 0$; positive values indicate like atom segregation ($i = j$), while negative values imply ordering between unlike species ($i \neq j$). The fcc simulation cell used contained 2916 atoms.

The MTP potential reproduces the overall CSRO trends reported by DFT, though with reduced magnitudes. Table VII provides a comprehensive comparison of first-nearest-neighbor Warren-Cowley short-range order parameters across temperatures (1200 K, 800 K, and 500 K) for CoCrNi and CoCrFeNi alloys. Several important trends emerge when analyzing the temperature evolution and model to model consistency. For both alloys, DFT shows the expected thermodynamic behavior: CSRO magnitudes increase as temperature decreases. At 1200 K, most α_{ij} values are modest, indicating weak ordering tendencies. As temperature decreases to 800 K and further to 500 K, like-atom clustering (positive α_{ii}) and unlike-atom ordering (negative α_{ij}) intensify. For example, in CoCrNi, Cr–Cr clustering increases from 0.14 (1200 K) to 0.42 (500 K), while Ni–Cr ordering strengthens from –0.12 to –0.27. A similar amplification is observed in CoCrFeNi, where Cr–Cr clustering remains strong ($0.65 \rightarrow 0.59$) and Fe–Fe clustering increases substantially ($0.17 \rightarrow 0.54$). This monotonic temperature strengthening reflects physically consistent ordering thermodynamics. The EAM potential exhibits qualitatively incorrect chemical tendencies at low temperature. At 500 K, EAM predicts strong Ni–Cr repulsion (+0.38), directly contradicting the DFT predicted attraction (–0.27). Similarly, Cr–Cr clustering becomes negative (–0.11), implying repulsion rather than clustering. EAM also dramatically overestimates Ni–Ni clustering (0.47 vs 0.12 in DFT), artificially promoting elemental segregation. These sign reversals and exaggerated magnitudes indicate that the empirical embedding framework does not capture the underlying electronic-driven chemical affinity landscape in Cr-containing alloys. MEAM improves certain aspects but still struggles with sign fidelity. In CoCrNi at 500 K, MEAM predicts Cr–Cr to be strongly negative (–0.29), reversing the DFT clustering tendency (+0.42). It also inverts Cr–Co ordering and underestimates Ni–Cr attraction. The situation is more pronounced in CoCrFeNi, where MEAM inverts multiple key interactions across all temperatures (e.g., Cr–Cr, Cr–Co, Cr–Fe, Co–Fe). The frequent sign flips imply a qualitatively different chemical ordering landscape, which would significantly alter predicted defect energetics and phase stability.

The MTP-Cao model exhibits intermediate behavior. While it captures some sign trends in CoCrNi (e.g., Ni–Cr ordering), it underestimates magnitudes and struggles to reproduce consistent temperature amplification. In particular, the damping is more pronounced than in the present MTP, and certain interactions (e.g., Ni–Ni at high temperature) show incorrect sign tendencies. This suggests limited transferability when the training database does not fully constrain multicomponent chemical environments. The present MTP consistently reproduces the sign structure of DFT across all temperatures and both alloy systems. In CoCrNi, Ni–Cr remains negative at all temperatures and Cr–Cr remains positive, with magnitudes increasing toward lower temperature, mirroring DFT trends. In CoCrFeNi, all dominant chemical tendencies, including strong Cr–Cr clustering and Ni–Fe ordering, are correctly captured. Although the magnitudes are systematically reduced relative to DFT, the temperature dependence and pairwise ranking are preserved. The magnitude damping likely reflects a combination of larger supercell sampling, longer MC/MD trajectories, and the absence of explicit spin degrees of

TABLE VII. First-nearest-neighbor WC short-range order parameters α_{ij} (dimensionless) for equiatomic CoCrNi and CoCrFeNi at 1200 K, 800 K, and 500 K. Positive α_{ij} indicates like-species clustering, while negative values indicate chemical ordering between unlike species.

CoCrNi

Pair	DFT	EAM	MEAM	MTP-Cao	MTP
			1200 K		
Ni-Ni	0.07	−0.10	0.02	−0.03	0.00
Ni-Cr	−0.12	0.04	0.01	0.01	−0.10
Ni-Co	0.05	0.16	−0.05	0.05	0.10
Cr-Cr	0.14	0.12	−0.11	0.03	0.08
Cr-Co	−0.03	−0.28	0.21	−0.07	−0.06
Co-Co	−0.03	0.06	−0.08	0.01	−0.02
			800 K		
Ni-Ni	0.03	−0.22	0.02	−0.07	0.00
Ni-Cr	−0.15	0.13	−0.02	0.01	−0.12
Ni-Co	0.13	0.30	−0.02	0.13	0.13
Cr-Cr	0.28	0.12	−0.13	0.07	0.13
Cr-Co	−0.12	−0.38	0.28	−0.16	−0.14
Co-Co	0.00	0.04	−0.13	0.02	0.01
			500 K		
Ni-Ni	0.12	0.47	0.03	−0.06	0.01
Ni-Cr	−0.27	0.38	0.03	−0.07	−0.17
Ni-Co	0.15	0.57	−0.09	0.20	0.16
Cr-Cr	0.42	−0.11	−0.29	0.15	0.19
Cr-Co	−0.16	−0.57	0.56	−0.24	−0.21
Co-Co	0.01	−0.08	−0.23	0.02	0.02

CoCrFeNi

Pair	DFT	MEAM	MTP
		1200 K	
Ni-Ni	0.13	0.01	−0.01
Ni-Cr	−0.22	0.01	−0.07
Ni-Co	0.12	0.07	0.13
Ni-Fe	−0.04	−0.11	−0.02
Cr-Cr	0.65	−0.17	0.06
Cr-Co	−0.26	0.26	−0.07
Cr-Fe	−0.17	0.23	−0.02
Co-Co	0.11	−0.05	−0.01
Co-Fe	0.03	−0.19	−0.02
Fe-Fe	0.17	0.02	0.02
		800 K	
Ni-Ni	0.16	0.02	−0.01
Ni-Cr	−0.21	0.16	−0.06
Ni-Co	0.10	−0.02	0.17
Ni-Fe	−0.04	−0.20	−0.08
Cr-Cr	0.54	−0.47	0.08
Cr-Co	−0.18	0.60	−0.13
Cr-Fe	−0.14	0.64	−0.06
Co-Co	0.13	−0.08	−0.01
Co-Fe	−0.05	−0.35	−0.01
Fe-Fe	0.23	−0.03	0.05
		500 K	
Ni-Ni	0.30	0.03	0.06
Ni-Cr	−0.18	0.36	−0.24
Ni-Co	0.14	−0.11	0.37
Ni-Fe	−0.27	−0.33	−0.31
Cr-Cr	0.59	−0.66	0.24
Cr-Co	−0.31	0.79	−0.29
Cr-Fe	−0.10	0.83	−0.21
Co-Co	0.33	−0.08	0.04
Co-Fe	−0.16	−0.45	−0.20
Fe-Fe	0.54	−0.02	0.24

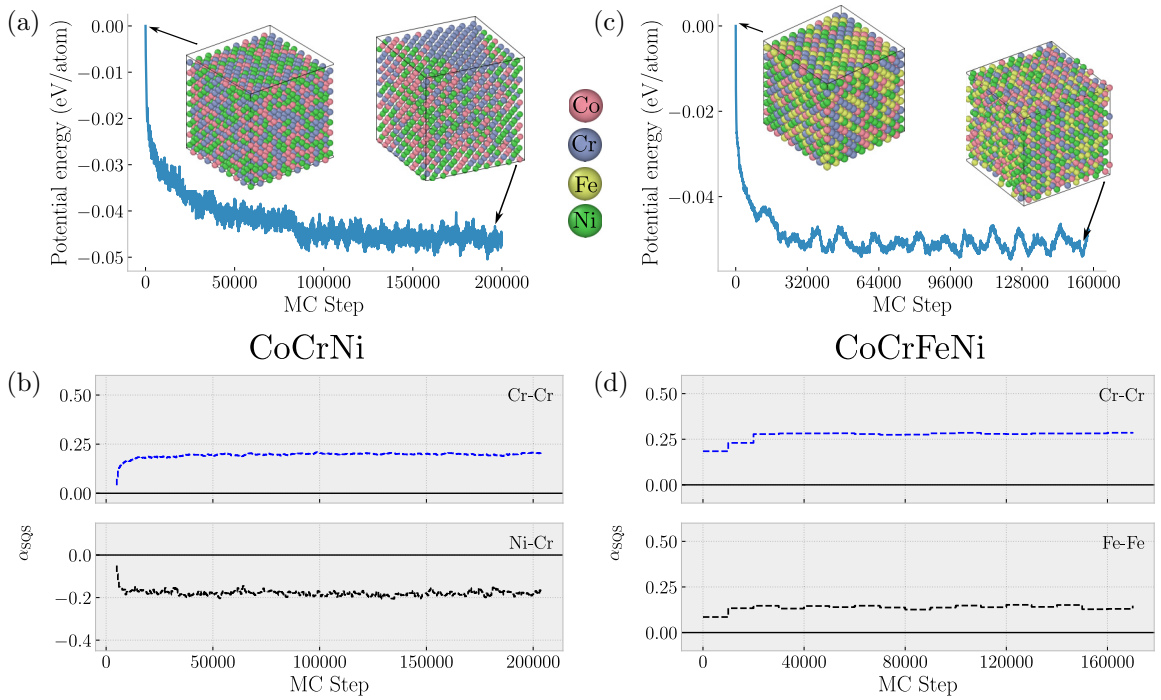

FIG. 9. Evolution of potential energy and CSRO during lattice MC simulations at 500 K. (a), (c) Potential energy convergence in CoCrNi and CoCrFeNi, respectively. (b), (d) Warren–Cowley CSRO parameters in the first-nearest-neighbor shell: (b) Cr–Cr and Ni–Cr in CoCrNi, (d) Cr–Cr and Fe–Fe in CoCrFeNi.

freedom in the potential energy functional. However, unlike EAM and MEAM, the present MTP does not invert interaction signs or artificially promote incorrect clusters.

The apparent reduction in CSRO magnitudes from MTP relative to DFT can plausibly arise from differences in system size and sampling. In our workflow, MTP permits substantially larger supercells (thousands of atoms) and many more MD steps between MC swaps, which in turn sample a wider spectrum of local environments, long-wavelength vibrational modes, and vibrational entropy contributions. By contrast, DFT calculations are necessarily constrained to smaller supercells and shorter trajectories, which can bias the statistics toward more pronounced CSRO values due to finite size effects. Accordingly, the discrepancies in α_{ij} magnitudes may reflect ensemble and size differences rather than model deficiency.

Figure 9 shows that in CoCrNi, Cr–Cr pairs exhibit positive α (repulsion), while Ni–Cr pairs show negative α (ordering), consistent with DFT predictions. For CoCrFeNi, both Cr–Cr and Fe–Fe interactions are repulsive, while Ni–Fe and Cr–Ni favor mixing. Compared with DFT, MTP underestimates the strength of like-atom repulsion, reflecting the absence of explicit spin-polarization and electronic structure fidelity. Nonetheless, it captures the qualitative chemical tendencies and provides reliable insight into CSRO evolution at large scales.

Figure 10 expands the analysis to multiple pairs and shells. In CoCrNi [Fig. 10(a)], MTP predicts positive α for like atom interactions (Cr–Cr, Ni–Ni) and negative α for dissimilar pairs (Cr–Ni, Co–Cr), while Co–Co and Co–Ni remain near random, consistent with DFT. For CoCrFeNi [Fig. 10(b)], the same pattern emerges: strong repulsion for Cr–Cr and Fe–Fe, ordering for Cr–Ni and Fe–Ni, and weak interactions for solvent-like pairs. Importantly, MTP correctly captures the relative trends of CSRO across the first shell, even if it underestimates absolute magnitudes.

5. *Stacking fault energy*

GSFE values were computed for CoCrNi-based systems using MTP and compared with DFT predictions obtained from SQS. Both random and CSRO configurations were considered within the MTP framework. Simulations were conducted by rigidly shifting the upper half of a supercell along the {111} glide plane in the ⟨112⟩ direction for CoCrFeNi and CoCrNi, generating discrete GSFE curves from 16 unique glide planes to ensure statistical reliability. The GSFE landscape was resolved by calculating both the γ_{usf}, corresponding to the peak barrier for dislocation nucleation, and γ_{isf}, reflecting post slip stability. For CSRO structures, configurations were pre-equilibrated via hybrid MD/MC annealing under a variance constrained semi-grand-canonical ensemble. The energy profiles were normalized with respect to slip displacement, and GSFE curves were constructed by sampling displacements over one Burgers vector periodicity.

Comparative analysis of MTP and DFT results indicates that CSRO enhances both γ_{usf} and γ_{isf}, suggesting increased resistance to dislocation motion and stabilization of the fcc phase, respectively. This trend underscores the significant role of local chemical environments in tailoring deformation mechanisms in complex alloys.

Figure 11 shows the GSFE obtained from the MTP demonstrates good qualitative agreement with DFT predictions but underestimates both the magnitude and variability of the ISF

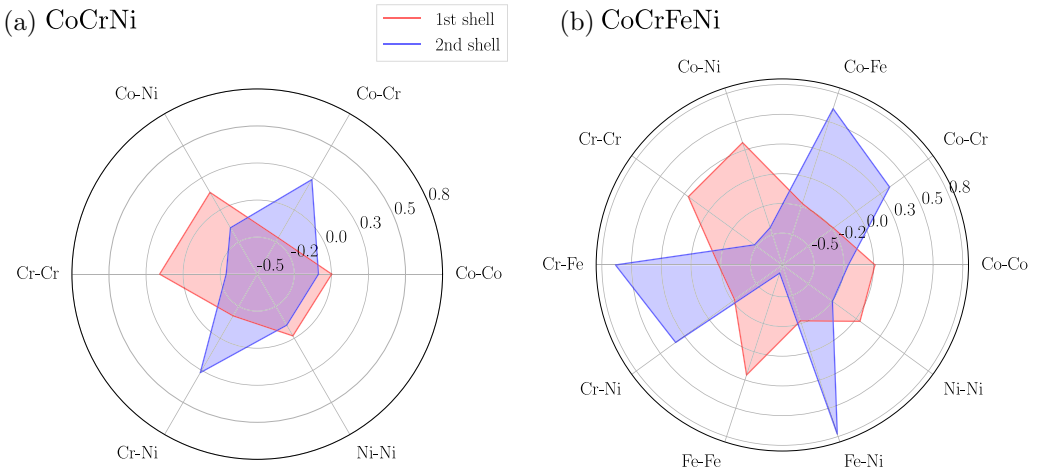

FIG. 10. Warren–Cowley CSRO parameters for first- and second-nearest-neighbor shells in (a) CoCrNi and (b) CoCrFeNi, obtained at the end of MTP-based hybrid MC/MD simulations at 500 K. Red regions correspond to the first shell, and blue regions the second shell. Positive values indicate like-atom repulsion, negative values indicate ordering between unlike species.

energy for CoCrNi. In DFT combined with MC simulations, CoCrNi exhibits an average $\gamma_{\text{isf}} \approx 80$ mJ/m^2 [96], with a broad distribution ranging from slightly negative values up to ∼288 mJ/m^2, strongly dependent on local chemical environments. MTP predicts a lower average value of $\gamma_{\text{isf}} \approx 54$ mJ/m^2, with a narrower spread of ∼40–65 mJ/m^2 across different fault planes. Despite this quantitative discrepancy, the MTP correctly captures the chemistry-dependent trends, where Co-rich fault planes exhibit reduced γ_{isf} while Cr-enriched planes elevate γ_{isf}, consistent with DFT results.

While DFT calculations with MC sampling predict an ISF energy in the range of 17–34 mJ/m^2 [97], the present MTP with CSRO configurations yields a value of $\gamma_{\text{isf}} \approx 35.6$ mJ/m^2, in excellent agreement with the upper bound of the DFT range. Unlike DFT, which is limited to a small number of local configurations, the MTP efficiently samples a wide spectrum of fault-plane chemistries and reveals that Fe- and Ni-rich planes favor higher γ_{isf}, whereas Co-rich environments suppress it. This chemical sensitivity, illustrated in Fig. 12, is consistent with first principles trends but accessible here on significantly larger length scales. Moreover, as summarized in Table VIII, the MTP reproduces the relative ordering of GSFE among CoCrFeNi and CoCrNi. These results underscore that the MTP framework offers a robust and computationally efficient pathway to probe the role of ISFs and CSRO in dictating plasticity in complex concentrated alloys.

MTP models, when trained carefully on diverse datasets including chemically perturbed structures, can qualitatively reproduce the sensitivity of GSFE to local chemical environment, a feature traditionally absent in empirical potentials such as MEAM [35] or LJ-type effective potentials [36].

6. Solute segregation in GB structure

Grain boundaries (GBs) play a central role in determining the mechanical strength, ductility, diffusion kinetics, corrosion resistance, and thermal stability of multicomponent alloys. In complex concentrated alloys, where multiple principal elements compete for local chemical environments, GB structure and chemistry are strongly coupled. Even subtle variations in CSRO can modify segregation tendencies, alter local atomic packing (e.g., kite units in Σ5 boundaries), and consequently change GB energy and mobility. Therefore, validating an interatomic potential against GB. In this work, a Σ5 (210) symmetric tilt grain boundary was constructed following the reference geometry shown in the attached study, with orientation relationships [100], [0 2 $\bar{1}$], and [0 1 $\bar{2}$]. The initial

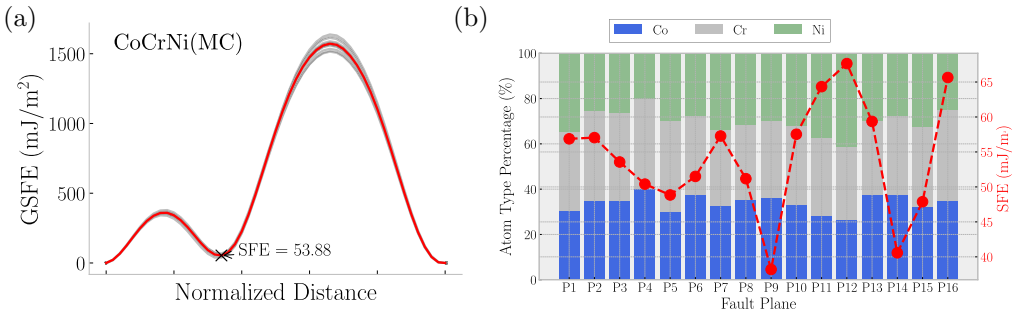

FIG. 11. Comparison of stacking fault energetics in CoCrNi obtained from the MC simulation using MTP. (a) Average GSFE curve along the ⟨112⟩/6 slip path, showing an ISF energy of $\gamma_{\text{isf}} \approx 53.9$ mJ/m^2. (b) Variation of γ_{isf} across different fault planes and the corresponding local atomic composition

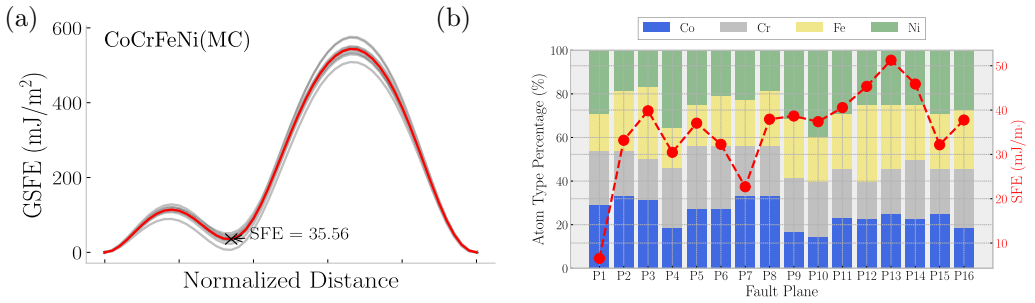

FIG. 12. GSFE of CoCrFeNi obtained from the MTP with CSRO configurations. (a) Average GSFE curve along the $\langle 112 \rangle/6$ slip path, yielding an ISF energy of $\gamma_{\mathrm{isf}} \approx 35.6$ mJ/m^2. (b) Plane-resolved variation of γ_{isf} across different fault planes along with the corresponding local atomic composition, showing clear chemistry-dependent fluctuations.

model consisted of a pure Ni GB containing 2000 atoms. Alloying was introduced by randomly substituting Ni atoms with Co and Cr (33% each) for CoCrNi, or Co/Cr/Fe (25% each) for CoCrFeNi, while preserving the overall composition. After full structural relaxation, hybrid MD–MC simulations were carried out at 25 K for 200 000 steps, using the same convergence protocol as in the CSRO calculations.

The segregation behavior further highlights differences in chemical ordering at the GB, as illustrated in Fig. 13. In CoCrNi, Cr atoms show a higher tendency to accumulate in the boundary core region relative to Co, consistent with their stronger chemical driving force for unlike-neighbor ordering observed in the bulk CSRO analysis. Quantitatively, the boundary-core composition differs noticeably from the nominal equiatomic concentration: for example, in the MTP case the GB region exhibits Ni enrichment (40.15%) accompanied by reduced Co content (22.01%) and moderate Cr concentration (37.84%), indicating selective site preference within the kite units. In contrast, the MTP-Cao model produces a substantially different redistribution (Co: 26.54%, Cr: 35.38%, Ni: 38.08%), which correlates with the structural reconstruction of the kite units into a diamondlike configuration.

For CoCrNi, classical EAM and the present MTP preserve the characteristic kite-shaped structural units of the Σ5 boundary after chemical equilibration, whereas MTP-Cao alters the local topology. The segregation percentages shown beneath each panel in Fig. 13 reveal that even moderate compositional shifts (on the order of 5–10 at.%) in the GB core are sufficient to destabilize the structural units if the chemical interactions are not properly balanced. The present MTP allows selective enrichment without triggering structural collapse, indicating a physically consistent coupling between segregation energetics and boundary topology. For CoCrFeNi, more pronounced differences emerge between potentials. MEAM leads to visible distortion of the kite structure (Fig. 13), suggesting that the angular bonding description and multicomponent chemical interactions are not simultaneously captured with sufficient fidelity.

In contrast, the present MTP preserves the kite topology and predicts chemically selective segregation trends consistent with bulk CSRO tendencies. In the quaternary alloy, the GB core composition shifts from the nominal 25% per element to approximately Co: 14.90%, Cr: 20.39%, Fe: 27.45%, and Ni: 37.25% in the MTP simulation. This indicates preferential enrichment of Ni and Fe at the boundary core, while Co is depleted. Such compositional redistribution modifies the local bonding environment of the kite units but does not induce artificial reconstruction. By comparison, MEAM produces larger deviations and structural distortion, indicating an imbalance between segregation driving forces and structural stability. GB structural units such as kite motifs directly control dislocation absorption, crack initiation resistance, impurity embrittlement, and diffusion pathways. A potential that artificially reconstructs these units can lead to qualitatively incorrect predictions of mechanical response and segregation-driven stabilization mechanisms.

The present MTP is not merely a tool for reproducing DFT level energies in bulk configurations; it enables physically meaningful large-scale simulations of chemically complex grain boundaries, where both structural fidelity and chemical ordering must be described simultaneously. The ability to maintain stable GB structural units while resolving segregation-driven compositional fluctuations on the order of 10–15 at. % from the nominal composition demonstrates that the potential is suitable for mesoscale studies of grain boundary engineering, thermally activated diffusion, and defect mediated plasticity in multicomponent alloys. These regimes remain computationally inaccessible to first principles methods but are critically important for understanding strength and stability in complex concentrated alloys.

TABLE VIII. Intrinsic stacking fault energies γ_{ISF} (mJ m^{-2}) for CoCrFeNi and CoCrNi, comparing DFT (SQS), empirical potentials (EAM/MEAM) for CSRO configurations where available, and MTP (CSRO). MTP values are reported as mean ± standard deviation across sampled CSRO structures.

System	DFT (SQS)	EAM (CSRO)	MEAM (CSRO)	MTP (CSRO)
CoCrFeNi	17–34 [97]	—	88.97 ± 8	35.56 ± 12
CoCrNi	80 [96]	72.56 ± 8	13.82 ± 6	53.88 ± 5

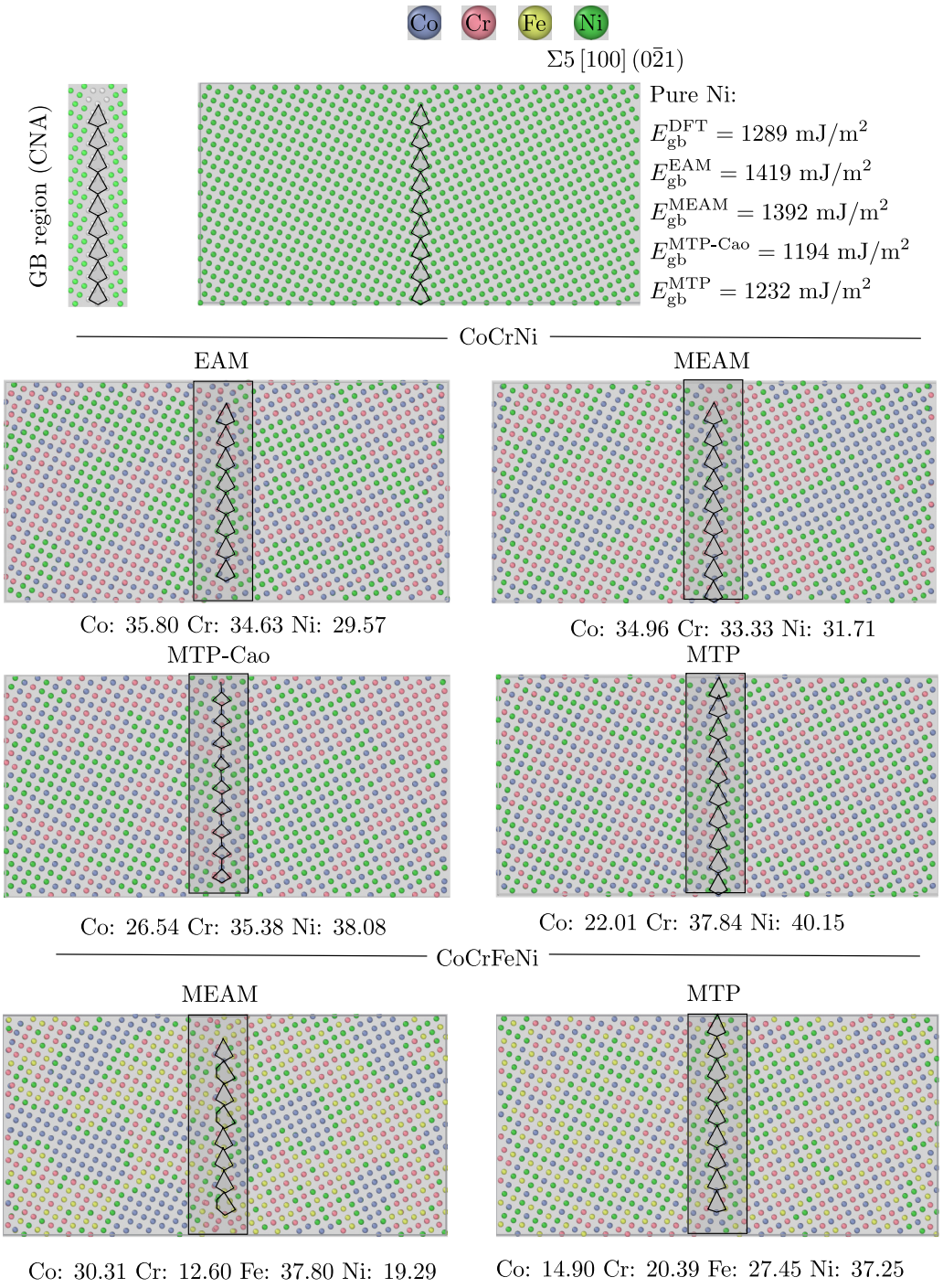

FIG. 13. Solute segregation and structural stability of the Σ5 (210) grain boundary (GB) in Ni-based multicomponent alloys after hybrid MD–MC equilibration at 25 K. Atoms are colored by species (Co: blue, Cr: red, Fe: yellow, Ni: green). The boxed region highlights the GB core containing the characteristic kite structural units. Top panel: Reference pure Ni GB with DFT and classical potential GB energies listed for comparison. Middle panels (CoCrNi): Results obtained using EAM, MEAM, MTP-Cao, and the present MTP. The numbers beneath each image indicate the local atomic percentages within the GB core region. Bottom panels (CoCrFeNi): Comparison between MEAM and the present MTP.

IV. CONCLUSION

The key findings can be summarized as follows:

(1) The MTP quantitatively reproduces the lattice constants and elastic constants of both CoCrNi and CoCrFeNi, achieving near-DFT accuracy and excellent agreement with experimental measurements. In contrast, classical empirical potentials such as EAM and MEAM systematically underestimate C_{44} and overestimate C_{12}, resulting in deviations in bulk modulus predictions. The superior accuracy of MTP highlights its ability to capture many-body interactions and chemical disorder effects absent in classical potentials.

(2) Although trained on equiatomic CoCrFeNi datasets, the MTP demonstrates robust predictive capability for nonequiatomic compositions. MC/MD simulations using MTP reproduce DFT predicted trends in bulk and shear moduli across a wide compositional space. Specifically, alloys with higher Fe content exhibit lower bulk moduli, while Co enrichment enhances shear modulus. These trends agree with DFT predictions, underscoring the MTP's reliability in capturing composition-dependent elastic behavior.

(3) The MTP simulations capture the essential features of CSRO in CoCrNi and CoCrFeNi. Consistent with DFT-informed MC studies, MTP predicts strong repulsion between like-species pairs such as Cr–Cr and Fe–Fe, and favorable ordering for dissimilar pairs such as Ni–Cr and Ni–Fe. While the magnitude of CSRO is underestimated relative to DFT due to the absence of explicit spin polarization in MTP, the relative chemical trends are faithfully reproduced. This capability demonstrates that MTP can capture the influence of CSRO on alloy energetics and stability, an essential feature for modeling thermodynamic and mechanical behavior at realistic length scales.

(4) The GSFE was systematically evaluated using MTP for both random and CSRO configurations. For CoCrFeNi, MTP predicts an ISF energy of $\sim$35.6 mJ/m^2, which falls within the upper bound of DFT predictions (17–34 mJ/m^2). For CoCrNi, MTP yields an ISF energy of $\sim$53.9 mJ/m^2, lower than the DFT value of $\sim$80 mJ/m^2 but consistent with the chemical trends reported by first principles studies. Importantly, MTP captures the sensitivity of ISF to local atomic chemistry, predicting that Co-rich planes reduce γ_{isf} whereas Cr- and Fe-enriched planes increase it. This chemically resolved description of GSFE is not achievable with conventional empirical potentials.

The present MTP establishes a robust and transferable framework for the atomistic modeling of CoCrFeNi- and CoCrNi-based MEAs. It effectively reconciles the accuracy of first principles methodologies with the computational efficiency of empirical potentials, thereby enabling predictive simulations at scales inaccessible to *ab initio* approaches. The potential demonstrates reliability in reproducing elastic properties, CSRO, and stacking fault energetics, which are central to understanding the deformation behavior of these alloys. Collectively, the results reinforce the emerging role of ML interatomic potentials as indispensable tools for the quantitative exploration of defect processes, thermodynamic stability, and mechanical response in complex concentrated alloys.

ACKNOWLEDGMENTS

The authors acknowledge computational resources from the LANL Advanced Simulation and Computing Program. This study received no funding.

DATA AVAILABILITY

The data that support the findings of this article are openly available [98].

[1] J.-W. Yeh, S.-K. Chen, S.-J. Lin, J.-Y. Gan, T.-S. Chin, T.-T. Shun, C.-H. Tsau, and S.-Y. Chang, Nanostructured high-entropy alloys with multiple principal elements: Novel alloy design concepts and outcomes, Adv. Eng. Mater. **6**, 299 (2004).

[2] J.-W. Yeh, Y.-L. Chen, S.-J. Lin, and S.-K. Chen, High-entropy alloys–A new era of exploitation, in, *Advanced Structural Materials II*, Materials Science Forum, Vol. 560 (Trans Tech Publ., Amsterdam, Netherlands, 2007, pp. 1–9.

[3] M. Laurent-Brocq, A. Akhatova, L. Perrière, S. Chebini, X. Sauvage, E. Leroy, and Y. Champion, Insights into the phase diagram of the CrMnFeCoNi high entropy alloy, Acta Mater. **88**, 355 (2015).

[4] P. P. Bhattacharjee, G. Sathiaraj, M. Zaid, J. Gatti, C. Lee, C.-W. Tsai, and J.-W. Yeh, Microstructure and texture evolution during annealing of equiatomic CoCrFeMnNi high-entropy alloy, J. Alloys Compd. **587**, 544 (2014).

[5] N. Stepanov, M. Tikhonovsky, N. Yurchenko, D. Zyabkin, M. Klimova, S. Zherebtsov, A. Efimov, and G. Salishchev, Effect of cryo-deformation on structure and properties of CoCrFeNiMn high-entropy alloy, Intermetallics **59**, 8 (2015).

[6] B. Cantor, I. T. Chang, P. Knight, and A. Vincent, Microstructural development in equiatomic multicomponent alloys, Mater. Sci. Eng. A **375-377**, 213 (2004).

[7] B. Gludovatz, A. Hohenwarter, D. Catoor, E. H. Chang, E. P. George, and R. O. Ritchie, A fracture-resistant high-entropy alloy for cryogenic applications, Science **345**, 1153 (2014).

[8] G. D. Sathiaraj and P. P. Bhattacharjee, Analysis of microstructure and microtexture during grain growth in low stacking fault energy equiatomic CoCrFeMnNi high entropy and Ni–60 wt.% Co alloys, J. Alloys Compd. **637**, 267 (2015).

[9] B. Gludovatz, E. P. George, and R. O. Ritchie, Processing, microstructure and mechanical properties of the CrMnFeCoNi high-entropy alloy, JOM **67**, 2262 (2015).

[10] W. Liu, Y. Wu, J. He, T. Nieh, and Z. Lu, Grain growth and the Hall–Petch relationship in a high-entropy FeCrNiCoMn alloy, Scr. Mater. **68**, 526 (2013).

[11] G. Laplanche, A. Kostka, O. Horst, G. Eggeler, and E. George, Microstructure evolution and critical stress for twinning in the CrMnFeCoNi high-entropy alloy, Acta Mater. **118**, 152 (2016).

[12] F. Otto, A. Dlouhý, C. Somsen, H. Bei, G. Eggeler, and E. P. George, The influences of temperature and microstructure on the tensile properties of a CoCrFeMnNi high-entropy alloy, Acta Mater. **61**, 5743 (2013).

[13] B. Schuh, F. Mendez-Martin, B. Völker, E. P. George, H. Clemens, R. Pippan, and A. Hohenwarter, Mechanical properties, microstructure and thermal stability of a nanocrystalline CoCrFeMnNi high-entropy alloy after severe plastic deformation, Acta Mater. **96**, 258 (2015).

[14] O. N. Senkov, G. B. Wilks, J. M. Scott, and D. B. Miracle, Mechanical properties of $Nb_{25}Mo_{25}Ta_{25}W_{25}$ and $V_{20}Nb_{20}Mo_{20}Ta_{20}W_{20}$ refractory high entropy alloys, Intermetallics **19**, 698 (2011).

[15] N. L. Okamoto, S. Fujimoto, Y. Kambara, M. Kawamura, Z. M. Chen, H. Matsunoshita, K. Tanaka, H. Inui, and E. P. George, Size effect, critical resolved shear stress, stacking fault energy, and solid solution strengthening in the CrMnFeCoNi high-entropy alloy, Sci. Rep. **6**, 35863 (2016).

[16] D. S. Aidhy, Chemical randomness, lattice distortion and the wide distributions in the atomic level properties in high entropy alloys, Comput. Mater. Sci. **237**, 112912 (2024).
[17] H. S. Oh, D. Ma, G. P. Leyson, B. Grabowski, E. S. Park, F. Körmann, and D. Raabe, Lattice distortions in the FeCoNiCrMn high entropy alloy studied by theory and experiment, Entropy **18**, 321 (2016).
[18] Z. Dong, S. Schönecker, W. Li, D. Chen, and L. Vitos, Thermal spin fluctuations in CoCrFeMnNi high entropy alloy, Sci. Rep. **8**, 12211 (2018).
[19] S. Liu, Y. Wu, H. Wang, J. He, J. Liu, C. Chen, X. Liu, H. Wang, and Z. Lu, Stacking fault energy of face-centered-cubic high entropy alloys, Intermetallics **93**, 269 (2018).
[20] K. V. Werner, M. Naeem, F. Niessen, L. Zhu, M. Villa, X.-L. Wang, and M. A. Somers, Experimental and computational assessment of the temperature dependency of the stacking fault energy in face-centered cubic high-entropy alloys, Acta Mater. **278**, 120271 (2024).
[21] R. Chang, W. Fang, J. Yan, H. Yu, X. Bai, J. Li, S. Wang, S. Zheng, and F. Yin, Microstructure and mechanical properties of CoCrNi-Mo medium entropy alloys: Experiments and first-principle calculations, J. Mater. Sci. Technol. **62**, 25 (2021).
[22] J. Kumar, M. Radhakrishnan, S. Palaniappan, K. M. Krishna, K. Biswas, S. Srinivasan, R. Banerjee, and N. B. Dahotre, Cr content dependent lattice distortion and solid solution strengthening in additively manufactured CoFeNiCrx complex concentrated alloys—A first principles approach, Mater. Today Commun. **40**, 109485 (2024).
[23] M. Fedorov, J. S. Wróbel, A. Fernández-Caballero, K. J. Kurzydłowski, and D. Nguyen-Manh, Phase stability and magnetic properties in fcc Fe-Cr-Mn-Ni alloys from first-principles modeling, Phys. Rev. B **101**, 174416 (2020).
[24] I. Moravcik, M. Zelený, A. Dlouhy, H. Hadraba, L. Moravcikova-Gouvea, P. Papež, O. Fikar, I. Dlouhy, D. Raabe, and Z. Li, Impact of interstitial elements on the stacking fault energy of an equiatomic CoCrNi medium entropy alloy: Theory and experiments, Sci. Technol. Adv. Mater. **23**, 376 (2022).
[25] S. Wang, T. Zhang, H. Hou, and Y. Zhao, The magnetic, electronic, and thermodynamic properties of high entropy alloy CrMnFeCoNi: A first-principles study, Phys. Status Solidi B **255**, 1800306 (2018).
[26] Q. Xu, H. Guan, S. Huang, and Z. Zhong, Comparative study of vacancy cluster formation in pure Ni, CoCrNi, and CoCrFeNi with a CoCrFeMnNi multicomponent system, J. Alloys Compd. **918**, 165747 (2022).
[27] S. Kang and A. Tamm, Density functional study of atomic arrangements in CrMnFeCoNi high-entropy alloy and their impact on vacancy formation energy and segregation, Comput. Mater. Sci. **230**, 112456 (2023).
[28] W. Chen, X. Ding, Y. Feng, X. Liu, K. Liu, Z. Lu, D. Li, Y. Li, C. Liu, and X.-Q. Chen, Vacancy formation enthalpies of high-entropy FeCoCrNi alloy via first-principles calculations and possible implications to its superior radiation tolerance, J. Mater. Sci. Technol. **34**, 355 (2018).
[29] Q. Xu, H. Guan, Z. Zhong, S. Huang, and J. Zhao, Irradiation resistance mechanism of the CoCrFeMnNi equiatomic high-entropy alloy, Sci. Rep. **11**, 608 (2021).
[30] D. Ma, B. Grabowski, F. Körmann, J. Neugebauer, and D. Raabe, *Ab initio* thermodynamics of the CoCrFeMnNi high entropy alloy: Importance of entropy contributions beyond the configurational one, Acta Mater. **100**, 90 (2015).
[31] C. Niu, A. Zaddach, C. Koch, and D. Irving, First principles exploration of near-equiatomic NiFeCrCo high entropy alloys, J. Alloys Compd. **672**, 510 (2016).
[32] M. S. Daw and M. I. Baskes, Embedded-atom method: Derivation and application to impurities, surfaces, and other defects in metals, Phys. Rev. B **29**, 6443 (1984).
[33] B.-J. Lee and M. I. Baskes, Second nearest-neighbor modified embedded-atom-method potential, Phys. Rev. B **62**, 8564 (2000).
[34] J. E. Jones, On the determination of molecular fields.—II. From the equation of state of a gas, Proc. R. Soc. London Ser. A **106**, 463 (1924).
[35] W.-M. Choi, Y. H. Jo, S. S. Sohn, S. Lee, and B.-J. Lee, Understanding the physical metallurgy of the CoCrFeMnNi high-entropy alloy: An atomistic simulation study, npj Comput. Mater. **4**, 1 (2018).
[36] R. Gröger, V. Vitek, and A. Dlouhý, Effective pair potential for random fcc CoCrFeMnNi alloys, Modell. Simul. Mater. Sci. Eng. **28**, 075006 (2020).
[37] V. L. Deringer, M. A. Caro, and G. Csányi, Machine learning interatomic potentials as emerging tools for materials science, Adv. Mater. **31**, 1902765 (2019).
[38] Y. Men, D. Wu, Y. Hu, L. Li, P. Li, S. Jia, J. Wang, G. Cheng, S. Chen, and W. Luo, Understanding alkaline hydrogen oxidation reaction on PdNiRuIrRh high-entropy-alloy by machine learning potential, Angew. Chem. Int. Ed. **62**, e202217976 (2023).
[39] Y. Zhou, P. Srinivasan, F. Körmann, B. Grabowski, R. Smith, P. Goddard, and A. I. Duff, Thermodynamics up to the melting point in a TaVCrW high entropy alloy: Systematic *ab initio* study aided by machine learning potentials, Phys. Rev. B **105**, 214302 (2022).
[40] H. Zheng, L. T. Fey, X.-G. Li, Y.-J. Hu, L. Qi, C. Chen, S. Xu, I. J. Beyerlein, and S. P. Ong, Multi-scale investigation of short-range order and dislocation glide in MoNbTi and TaNbTi multi-principal element alloys, npj Comput. Mater. **9**, 89 (2023).
[41] T. Wang, J. Li, M. Wang, C. Li, Y. Su, S. Xu, and X.-G. Li, Unraveling dislocation-based strengthening in refractory multi-principal element alloys, npj Comput. Mater. **10**, 143 (2024).
[42] M. S. Nitol, D. E. Dickel, and C. D. Barrett, Machine learning models for predictive materials science from fundamental physics: An application to titanium and zirconium, Acta Mater. **224**, 117347 (2022).
[43] M. S. Nitol, K. Dang, S. J. Fensin, M. I. Baskes, D. E. Dickel, and C. D. Barrett, Hybrid interatomic potential for Sn, Phys. Rev. Mater. **7**, 043601 (2023).
[44] Y. Zuo, C. Chen, X. Li, Z. Deng, Y. Chen, J. Behler, G. Csányi, A. V. Shapeev, A. P. Thompson, M. A. Wood, *et al.*, Performance and cost assessment of machine learning interatomic potentials, J. Phys. Chem. A **124**, 731 (2020).
[45] J. Behler, Perspective: Machine learning potentials for atomistic simulations, J. Chem. Phys. **145**, 170901 (2016).
[46] A. P. Bartók, M. C. Payne, R. Kondor, and G. Csányi, Gaussian approximation potentials: The accuracy of quantum mechanics, without the electrons, Phys. Rev. Lett. **104**, 136403 (2010).
[47] A. P. Thompson, L. P. Swiler, C. R. Trott, S. M. Foiles, and G. J. Tucker, Spectral neighbor analysis method for automated gen-

eration of quantum-accurate interatomic potentials, J. Comput. Phys. **285**, 316 (2015).
[48] A. V. Shapeev, Moment tensor potentials: A class of systematically improvable interatomic potentials, Multiscale Model. Simul. **14**, 1153 (2016).
[49] H. Kwon, M. Shiga, H. Kimizuka, and T. Oda, Accurate description of hydrogen diffusivity in bcc metals using machine-learning moment tensor potentials and path-integral methods, Acta Mater. **247**, 118739 (2023).
[50] J. Wang, P. Liu, H. Zhu, M. Liu, H. Ma, Y. Chen, Y. Sun, and X.-Q. Chen, Efficient moment tensor machine-learning interatomic potential for accurate description of defects in Ni-Al alloys, Phys. Rev. Mater. **9**, 053805 (2025).
[51] Y. Luo, J. A. Meziere, G. D. Samolyuk, G. L. Hart, M. R. Daymond, and L. K. Béland, A set of moment tensor potentials for zirconium with increasing complexity, J. Chem. Theory Comput. **19**, 6848 (2023).
[52] S. Yin, Y. Zuo, A. Abu-Odeh, H. Zheng, X.-G. Li, J. Ding, S. P. Ong, M. Asta, and R. O. Ritchie, Atomistic simulations of dislocation mobility in refractory high-entropy alloys and the effect of chemical short-range order, Nat. Commun. **12**, 4873 (2021).
[53] M. S. Nitol, A. Mishra, S. Xu, and S. J. Fensin, Moment tensor potential and its application in the Ti-Al-V multicomponent system, Phys. Rev. Mater. **9**, 063601 (2025).
[54] I. S. Novikov, K. Gubaev, E. V. Podryabinkin, and A. V. Shapeev, The MLIP package: Moment tensor potentials with MPI and active learning, Mach. Learn.: Sci. Technol. **2**, 025002 (2021).
[55] Y. Cao, K. Sheriff, and R. Freitas, Capturing short-range order in high-entropy alloys with machine learning potentials, npj Comput. Mater. **11**, 268 (2025).
[56] Q.-J. Li, H. Sheng, and E. Ma, Strengthening in multi-principal element alloys with local-chemical-order roughened dislocation pathways, Nat. Commun. **10**, 3563 (2019).
[57] S. P. Ong, W. D. Richards, A. Jain, G. Hautier, M. Kocher, S. Cholia, D. Gunter, V. L. Chevrier, K. A. Persson, and G. Ceder, Python materials genomics (pymatgen): A robust, open-source Python library for materials analysis, Comput. Mater. Sci. **68**, 314 (2013).
[58] P. Kumar and I. Adlakha, Effect of interstitial hydrogen on elastic behavior of metals: An *ab-initio* study, J. Eng. Mater. Technol. **145**, 011003 (2023).
[59] P. Mishra, P. Kumar, L. Neelakantan, and I. Adlakha, First-principles prediction of electrochemical polarization and mechanical behavior in Mg based intermetallics, Comput. Mater. Sci. **214**, 111667 (2022).
[60] A. Tamm, A. Aabloo, M. Klintenberg, M. Stocks, and A. Caro, Atomic-scale properties of Ni-based fcc ternary, and quaternary alloys, Acta Mater. **99**, 307 (2015).
[61] J. Hafner, *Ab-initio* simulations of materials using VASP: Density-functional theory and beyond, J. Comput. Chem. **29**, 2044 (2008).
[62] J. P. Perdew, K. Burke, and M. Ernzerhof, Generalized gradient approximation made simple, Phys. Rev. Lett. **77**, 3865 (1996).
[63] A. P. Thompson, H. M. Aktulga, R. Berger, D. S. Bolintineanu, W. M. Brown, P. S. Crozier, P. J. In't Veld, A. Kohlmeyer, S. G. Moore, T. D. Nguyen, *et al.*, LAMMPS—a flexible simulation tool for particle-based materials modeling at the atomic, meso, and continuum scales, Comput. Phys. Commun. **271**, 108171 (2022).
[64] A. Stukowski, Visualization and analysis of atomistic simulation data with OVITO–The open visualization tool, Modell. Simul. Mater. Sci. Eng. **18**, 015012 (2010).
[65] A. Chandran, A. Santhosh, C. Pistidda, P. Jerabek, R. C. Aydin, and C. J. Cyron, TiAlNb alloy interatomic potentials: Comparing passive and active machine learning techniques with MTP and DeepMD, Front. Mater. **12**, 1591955 (2025).
[66] K. Gubaev, V. Zaverkin, P. Srinivasan, A. I. Duff, J. Kästner, and B. Grabowski, Performance of two complementary machine-learned potentials in modelling chemically complex systems, npj Comput. Mater. **9**, 129 (2023).
[67] D. Farkas and A. Caro, Model interatomic potentials for Fe–Ni–Cr–Co–Al high-entropy alloys, J. Mater. Res. **35**, 3031 (2020).
[68] C. Kittel, *Kittel's Introduction to Solid State Physics, Global Edition* (Wiley, 2018).
[69] W. B. Pearson, *A Handbook of Lattice Spacings and Structures of Metals and Alloys*, International Series of Monographs on Metal Physics and Physical Metallurgy (Elsevier, 2013), Vol. 4.
[70] D. Antonangeli, M. Krisch, G. Fiquet, D. L. Farber, C. M. Aracne, J. Badro, F. Occelli, and H. Requardt, Elasticity of cobalt at high pressure studied by inelastic x-ray scattering, Phys. Rev. Lett. **93**, 215505 (2004).
[71] W. M. Haynes, D. R. Lide, and T. J. Bruno, *CRC Handbook of Chemistry and Physics : A Ready-Reference Book of Chemical and Physical Data* (CRC Press, Boca Raton, 2016).
[72] M. M. Choy, A. M. Hellwege, and K. H. Hellwege, *Elastic, Piezoelectric, Pyroelectric, Piezooptic, Electrooptic Constants, and Nonlinear Dielectric Susceptibilities of Crystals*, Zahlenwerte und Functionen aus Naturwissenschaften und Technik, neue Serie. Gruppe III, Kristall- und Festkörperphysik (Springer, 1979).
[73] P. Olsson, J. Wallenius, C. Domain, K. Nordlund, and L. Malerba, Two-band modeling of α-prime phase formation in Fe-Cr, Phys. Rev. B **72**, 214119 (2005).
[74] K. Lejaeghere, V. Van Speybroeck, G. Van Oost, and S. Cottenier, Error estimates for solid-state density-functional theory predictions: An overview by means of the ground-state elemental crystals, Crit. Rev. Solid State Mater. Sci. **39**, 1 (2014).
[75] J. J. Adams, D. S. Agosta, R. G. Leisure, and H. Ledbetter, Elastic constants of monocrystal iron from 3 to 500K, J. Appl. Phys. **100**, 113530 (2006).
[76] N. S. Kanhe, A. Kumar, S. Yusuf, A. Nawale, S. Gaikwad, S. A. Raut, S. Bhoraskar, S. Y. Wu, A. Das, and V. Mathe, Investigation of structural and magnetic properties of thermal plasma-synthesized $Fe_{1-x}Ni_x$ alloy nanoparticles, J. Alloys Compd. **663**, 30 (2016).
[77] G. Simmons, Single crystal elastic constants and calculated aggregate properties, J. Graduate Res. Center **34**, 1 (1965).
[78] M. R. LaBrosse, L. Chen, and J. K. Johnson, First principles study of vacancy and tungsten diffusion in fcc cobalt, Modell. Simul. Mater. Sci. Eng. **18**, 015008 (2010).
[79] S. Dudarev, Density functional theory models for radiation damage, Annu. Rev. Mater. Res. **43**, 35 (2013).
[80] A. R. Warwick, P.-W. Ma, and S. L. Dudarev, Point defect structures in hexagonal close packed metals and across the periodic table, Phys. Rev. Mater. **9**, 093605 (2025).

[81] C. Domain and C. S. Becquart, *Ab initio* calculations of defects in Fe and dilute Fe-Cu alloys, Phys. Rev. B **65**, 024103 (2001).

[82] X. Gong, Z. Li, A. S. Pattamatta, T. Wen, and D. J. Srolovitz, An accurate and transferable machine learning interatomic potential for nickel, Commun. Mater. **5**, 157 (2024).

[83] H. Lin, J.-X. Liu, H. Fan, and W.-X. Li, Compensation between surface energy and HCP/fcc phase energy of late transition metals from first-principles calculations, J. Phys. Chem. C **124**, 11005 (2020).

[84] R. Soulairol, C.-C. Fu, and C. Barreteau, Magnetic and energetic properties of low-index Cr surfaces and Fe/Cr interfaces: A first-principles study, Phys. Rev. B **84**, 155402 (2011).

[85] J. Yu, X. Lin, J. Wang, J. Chen, and W. Huang, First-principles study of the relaxation and energy of bcc-Fe, fcc-Fe and AISI-304 stainless steel surfaces, Appl. Surf. Sci. **255**, 9032 (2009).

[86] B. Sadigh, P. Erhart, A. Stukowski, A. Caro, E. Martinez, and L. Zepeda-Ruiz, Scalable parallel Monte Carlo algorithm for atomistic simulations of precipitation in alloys, Phys. Rev. B **85**, 184203 (2012).

[87] S. Mubassira, M. Fani, A. Raj, C. Hirt, R. S. Brinlee, A. Poozesh, W.-R. Jian, S. Z. Chavoshi, C. Lee, and S. Xu, Chemical short-range order and its influence on selected properties of non-dilute random alloys, Comput. Mater. Sci. **248**, 113587 (2025).

[88] M. Mizuno, K. Sugita, and H. Araki, Prediction of short-range order in CrMnFeCoNi high-entropy alloy, Results Phys. **34**, 105285 (2022).

[89] R. Zhang, S. Zhao, J. Ding, Y. Chong, T. Jia, C. Ophus, M. Asta, R. O. Ritchie, and A. M. Minor, Short-range order and its impact on the CrCoNi medium-entropy alloy, Nature (London) **581**, 283 (2020).

[90] X. Chen, Q. Wang, Z. Cheng, M. Zhu, H. Zhou, P. Jiang, L. Zhou, Q. Xue, F. Yuan, J. Zhu, *et al.*, Direct observation of chemical short-range order in a medium-entropy alloy, Nature (London) **592**, 712 (2021).

[91] H. Ge, H. Song, J. Shen, and F. Tian, Effect of alloying on the thermal-elastic properties of 3D high-entropy alloys, Mater. Chem. Phys. **210**, 320 (2018).

[92] M. Lucas, L. Mauger, J. Munoz, Y. Xiao, A. Sheets, S. Semiatin, J. Horwath, and Z. Turgut, Magnetic and vibrational properties of high-entropy alloys, J. Appl. Phys. **109**, 07E307 (2011).

[93] G. Laplanche, M. Schneider, F. Scholz, J. Frenzel, G. Eggeler, and J. Schreuer, Processing of a single-crystalline CrCoNi medium-entropy alloy and evolution of its thermal expansion and elastic stiffness coefficients with temperature, Scr. Mater. **177**, 44 (2020).

[94] W. Schweika and H.-G. Haubold, Neutron-scattering and Monte Carlo study of short-range order and atomic interaction in $Ni_{0.89}Cr_{0.11}$, Phys. Rev. B **37**, 9240 (1988).

[95] B. Schönfeld, L. Reinhard, G. Kostorz, and W. Bührer, Short-range order and atomic displacements in Ni–20 at% Cr single crystals, physica status solidi (b) **148**, 457 (1988).

[96] L. Zhu and Z. Wu, Effects of short range ordering on the generalized stacking fault energy and deformation mechanisms in fcc multiprincipal element alloys, Acta Mater. **259**, 119230 (2023).

[97] A. Zaddach, C. Niu, C. Koch, and D. Irving, Mechanical properties and stacking fault energies of NiFeCrCoMn high-entropy alloy, JOM **65**, 1780 (2013).

[98] https://gitlab.com/mtp_potentials/cocrfeni.